MSc Physics
Advanced Matter and Energy Physics

Master Thesis

Size-Dependent Open-Circuit Voltage in Lead Sulfide Colloidal Quantum Dot Solar Cells

---

by

Ruirt Bosma
10964746

April 2017
60 ECTS
March 2016 – March 2017

Supervisor/Examiner:
Dr. Bruno Ehrler

Examiner:
Prof. dr Albert Polman

Acknowledgements

First, I would like to thank everyone who helped realize this project. My foremost thanks go to Bruno Ehrler for giving me the opportunity to do research in the Hybrid Solar Cells group at AMOLF and for his great supervision during my time there. I admired that for any question I had there was always an answer or another question that would help me advance with my project. Being part of the Hybrid Solar Cell group was fun and inspiring and I would like to thank everyone in the group for good times during lunch and for useful discussions. Particular thanks go to Jumin Lee, who was often the first I looked to for guidance in and around the lab and who was always wiling to help. I would also like to thank Marc Duursma for his general lab support and for providing a safe and pleasant working environment. In addition to the everyone who helped with the science, I would like to thank my parents for their support throughout my entire studies, and finally I would like to thank Anne for making everything worthwhile.

Abstract

Colloidal quantum dots (CQDs) are a promising material for a wide range of optoelectronic devices, including solar cells. Particularly, the CQD size-dependent and highly tunable bandgap makes CQDs an interesting material for solar cells. However, for efficient solar cell device engineering it is important to have accurate knowledge of how the optoelectronic properties and energetics change with CQD size. Here, we study the optoelectronic properties of bilayer PbS CQD:C_{60} heterojunction solar cells fabricated with a range of CQD sizes. In particular, we address the PbS CQD size-dependent open-circuit voltage (V_{oc}) of these solar cells. The V_{oc}, determined by the quasi-Fermi level difference of holes and electrons, in these solar cells is limited by the discrete C_{60} LUMO and the PbS CQD valence band. Resulting changes in the V_{oc} with CQD size therefore depend only on the change in properties of the PbS CQDs. We find from the J-V characteristics that there is a strong PbS CQD size-dependent V_{oc}. This strong CQD size-dependent V_{oc} is not well-explained by the expected changes in the valence band with PbS CQD size, as measured with standard ultraviolet photoelectron spectroscopy (UPS) and X-ray photoelectron spectroscopy (XPS) found in literature. In addition, transient photovoltage (TPV) measurements are performed and show that the PbS CQD size dependence of the V_{oc} is also not due to differences in recombination rates. However, good agreement is found between the measured V_{oc} and a recently proposed UPS/XPS analyses method, as well as an method using field-effect transistors and ab-initio calculations to determine the valence band edge. These results suggest that the standard analysis of UPS and XPS is not accurate for PbS CQDs.

Table of contents

Chapter 1

Introduction

The rapidly increasing global energy demand, threat of climate change[1] and finite, fast depleting traditional energy sources, require a transformation of the global energy system. This transformation could be achieved by utilizing the most abundant energy source available on earth, solar energy. Each hour the sun delivers enough energy on earth to provide the global energy demand for a full year[2]. Besides being a clean and sustainable energy source, also the cost of solar energy from direct conversion of sunlight into electricity (photovoltaics) is becoming increasingly competitive with fossil fuels. However, conventional single junction silicon solar cells are closing in on their theoretical efficiency limit[3,4] and new developments are required to further increase the efficiency whilst minimizing the cost.

Colloidal quantum dots (CQDs) are solution-processed semiconductor nanocrystals with highly tunable optoelectronic properties, and could enable cheap multi-junction solar cells and overcome the efficiency limit of a single junction by harvesting a larger portion of the solar spectrum[5,6]. Particularly exciting is the use of CQDs as a back cell in multi-junction solar cells with existing silicon solar cell technologies or new emerging perovskite solar cell technologies as the top cell[7].

In recent years, CQD solar cell performance has rapidly improved, currently reaching a certified record efficiency of 12%[8].This rapid improvement in efficiency of the CQD solar cells over the past years is mainly due to two factors. The first factor is the improvement in the surface management of the relatively large surface area of the CQDs. Better passivation of the CQD surface has led to reduced trap state density and improved charge carrier transport, resulting in more efficient and stable CQD solar cells[9–13]. Secondly, there have been many developments in the device architecture[11,14–17]. Improvements in the top and bottom electrode selection, electron- and hole-acceptor layers, and importantly in the engineering of the band structure, have led to more stable solar cells, better charge extraction, increased light absorption and higher solar cell voltages.

While CQD solar cells have seen a remarkable increase in performance, there is still much room for improvement. CQD solar cells suffer from a relatively large voltage and current loss when compared with other photovoltaic materials[18]. The insufficient charge extraction and thus lower current in CQD solar cells is mainly due to recombination and poor charge carrier transport, which limits the device thickness and results in incomplete light absorption. The main efficiency loss in CQD solar cells comes from the voltage deficit, which is caused by the CQD size dispersity and by recombination due to the large surface-to-volume ratio.

Further improvement on these losses in the voltage and current of CQD solar cells can by achieved by reducing recombination with improved passivation and increasing the charge extraction with better band structure engineering[7]. This means that determination of the energies associated with the valence and conduction band of the PbS CQDs is important for fabrication of improved devices. Determination of the PbS CQD valence band edge is often performed by photoelectron spectroscopy[19] However, there are indications that this well-established technique for many semiconductor materials might not be accurate when applied to lead chalcogenides (PbS and PbSe)[20].

Here, we examine how the voltage, recombination and valence band edge in PbS CQD solar cells (the most efficient type of CQDs for solar cells to date) change with CQD size. In order to study these properties we fabricate bilayer heterojunction PbS CQD:C_{60} solar cells with different sized quantum dots. The open-circuit voltage (V_{oc}) depends on the difference in quasi-Fermi energy of the electrons and holes. In the heterojunction solar cells cell architecture, this quasi-Fermi energy difference is limited by the the diagonal bandgap. Here, the diagonal bandgap is the difference between the PbS CQD valence band edge and the lowest unoccupied molecular orbital (LUMO) of C_{60} . Additionally, the V_{oc} depends on the recombination in solar cells. The combination of V_{oc} and recombination measurements can therefore be used a a probe for the valence band edge change with CQD size.

The following chapter (2) comprises of a introduction into the principles of solar cells, quantum dots and quantum dot solar cells. Chapter 3 explains the methods and materials used for PbS CQD synthesis, solar cell fabrication and solar cell characterization. In Chapter 4 we present the characterization of the PbS CQD solar cells and compare our results with techniques used to determine the valence band edge of PbS CQDs.

Chapter 2

Background

2.1 Solar Cells

Solar cells are made of semiconductor materials that convert sunlight into electrical energy. The characteristics of these semiconductor materials can be described by the band model. In this model the energy of electrons in covalent bonds corresponds to the valence band, whereas the energy of unbound electrons corresponds to the conduction band[21]. In semiconductor materials and insulators these two bands are separated by a bandgap and the Fermi level, i.e. the energy that has an 50% chance of being occupied by an electron, lies in this bandgap, whereas in metals there is no bandgap and the Fermi level lies within the bands. These bands are close to the Fermi level in semiconductor materials and the bandgap is relatively small. This is utilized by solar cells were the photovoltaic effect, in which light promotes an electron across the bandgap, is used to generate electricity.

The sun is a blackbody radiator and the solar irradiance covers a broad spectrum of photon energies (figure 2.1). In a single junction solar cell photons with an energy larger than the semiconductor bandgap are absorbed by the semiconductor material, however photons with an energy smaller than the bandgap are not absorbed and their energy is lost[18]. The absorbed photons then promote electrons from the valence band into the conduction band, leaving behind holes in the valence band. Here, another part of the solar energy is lost as the charge carriers, created by photons with an energy larger than the bandgap, relax to the band edges, losing their excess energy through thermal radiation. These charge carriers then need to be separated and extracted from the semiconductor material, by transporting the holes and electrons to different contacts.
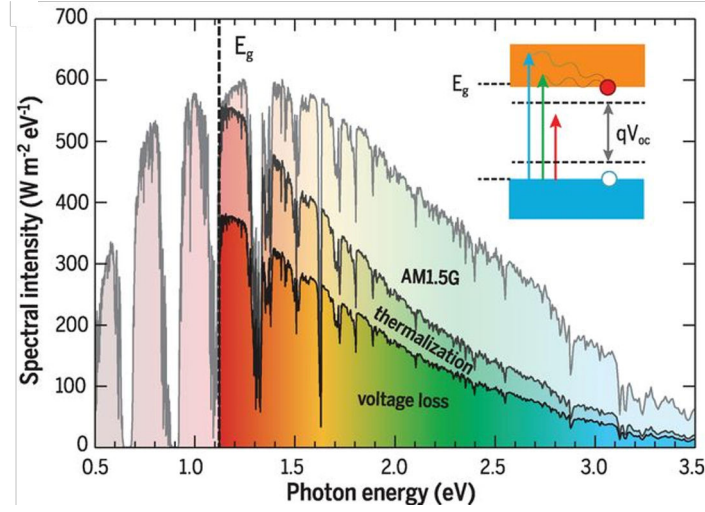
Fig. 2.1 Solar spectrum with losses from incomplete absorption due to photons with an energy lower than the bandgap not being absorbed, thermalization of the charge carriers with excess energy and voltage loss due to detailed balance. Inset shows schematic band diagram including losses from unabsorbed photons, photons with an energy larger than the bandgap and voltage loss. Figure taken from Polman et al.[18].

2.1.1 Fundamentals

The most common solar cells use silicon as the semiconductor material in a p-n junction architecture. This architecture joins a p-type semiconductor, in which the holes are the majority carriers, and a n-type semiconductor, in which the electrons are the majority carriers. When the two types of semiconductor are brought in contact the diffusion of electrons and holes results in the formation of a depletion region at the junction. In this depletion region an electric field builds up and in thermal equilibrium the drift current from this field balances the diffusion current[21,22]. A p-n junction solar cell can be described as a diode under illumination (Figure 2.2) and the current-voltage (J-V) characteristics of this solar cell in the dark can therefore be described by the ideal diode equation[21]:

$$J = J_0(e^{\frac{qV}{nkT}} - 1) \tag{2.1}$$

where J is the current density, J_0 is the dark saturation current density, q the elementary charge, n the idealty factor, T the temperature, k the Boltzmann constant and V the applied voltage.

The current from carriers generated when a solar cell is illuminated adds to the dark current and the diode equation becomes

$$J = J_0(e^{\frac{qV}{nkT}} - 1) - J_{\mathrm{L}} \tag{2.2}$$
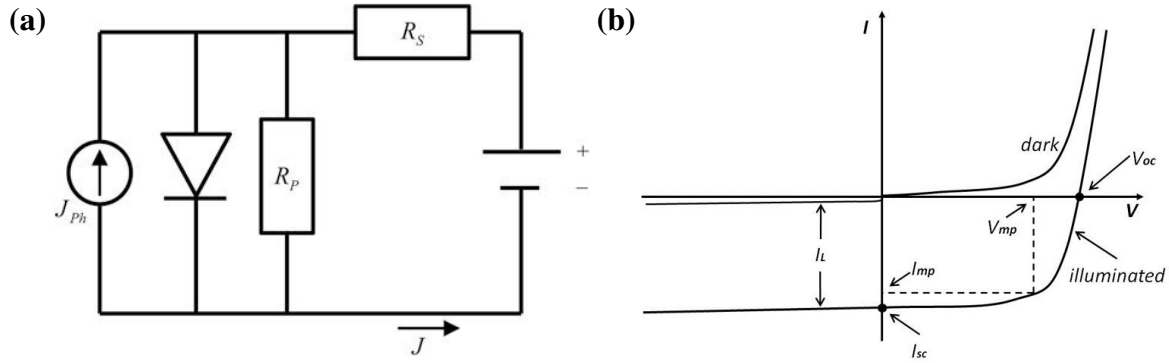
Fig. 2.2 (a) Schematics of a solar cell depicted as a diode under illumination. In a real solar cell there are also additional losses from shunt resistance R_p and series resistance R_s, both also depicted. Figure taken from Borchert[19].(b) IV-curves of a solar cell in the dark and under illumination, showing the illumination current I_L, current at maximum powerpoint I_{mp}, short-circuit current I_{sc}, voltage at maximum powerpoint V_{mp} and open-circuit voltage V_{oc}

with J_L the illumination current density. The corresponding I-V curve (Figure 2.2) is used to characterize the solar cell and shows several important parameters. The short-circuit current density J_{sc} is the current on the cell when the contacts are shorted, there is no voltage on the cell and the current generated is at its maximum. The maximum voltage a solar cell can generate is the open-circuit voltage V_{oc}, which occurs when there is no current going through the solar cell.

The maximum power P_{mp} and corresponding voltage and current at the maximum point point (V_{mp} and J_{mp}) that a solar cell can produce depends on the quality of the solar cell and can graphically be depicted as the largest square that fits in the J-V curve (figure 2.2). Another important parameter here is the fill factor (FF), which is the ratio of this square to the product of V_{oc} and J_{sc}. The power conversion efficiency η of the solar cell, which is defined as the maximum power divided by the incident power from the sunlight, is then as follows:

$$\eta = \frac{P_{mp}}{P_{in}} = \frac{V_{mp}J_{mp}}{P_{in}} = \frac{V_{oc}J_{sc}FF}{P_{in}} \tag{2.3}$$

2.1.2 Open-Circuit Voltage and Recombination

Equation 2.2 shows that when there is no current extracted from the solar cells ($J = 0$) than the relation between V_{oc}, J_{sc} and J_0 can be described by,

$$V_{oc} = \frac{nkT}{q} ln\left(\frac{J_L}{J_0} + 1\right) \tag{2.4}$$

and since $\frac{J_L}{J_0} >> 1$,

$$V_{oc} \approx \frac{nkT}{q} ln\left(\frac{J_{sc}}{J_0}\right) \tag{2.5}$$

where the approximation $J_L \approx J_{sc}$ holds if the solar cell is reasonably described by an ideal diode. In a p-n junction solar cell, the difference between the quasi-fermi level of the electrons in the n-type semiconductor and the holes in the p-type semiconductor determines the V_{oc}. This difference is limited by the semiconductor bandgap and depends on the charge recombination in the solar cell.

Several types of recombination can be distinguished. The first, and fundamentally present in every solar cell, is radiative recombination. Radiative recombination is fundamentally required from detailed balance, which says that in equilibrium the processes in a system are balanced by their reverse. For a solar cell in thermal equilibrium this means that absorption of photons, and the creation of electron-hole pairs, is balanced by recombination of electron and holes, and thus emission of photons[3]. Another type of recombination that can contribute to the dark saturation current J_0 is Auger recombination[21]. In this type of recombination and electron and hole also recombine, however the energy is not emitted by a photon, but transfered to a different electron which can then release this energy thermally, by relaxing to the conduction band edge. The third type of recombination is trap-assisted recombination. This type of recombination is caused by impurities and defects at the interfaces or inside of the semiconductor material. These defects cause trap states in the bandgap which allows the carriers to first relax to the trap state before recombining,increasing the chance of recombination as the trap state sits deeper in the band gap. Furthermore, charges carriers in these trap states can not be extracted, adding to the the dark saturation current.

In short, several types of recombination contribute to the dark saturation current J_0, and reduce the V_{oc} of a solar cell. Radiative recombination is fundamentally present and depends on the solar cell bandgap. In addition to radiative recombination, the dark saturation current J_0 is also increased by non-radiative recombination processes, such as Auger recombination and trap-assisted recombination, that depend on defects in the material.

2.2   Colloidal Quantum Dot Solar Cells

2.2.1   Colloidal Quantum Dots

Solution-processed colloidal quantum dots are interesting for solar cells[23,24], but also for other optoelectronic devices such as, photodetectors[25,26], light emitting diodes[27,28], biomedical sensors[29], because of their optoelectronic tunability. The unique optoelectronic properties of

these nanometer-sized semiconductor crystallites, called colloidal quantum dots, arises from their small size. At these small sizes, when the semiconductor radius becomes smaller than the Bohr radius of the electrons and holes, there is strong confinement of the exciton (bound electron and hole)[30]. In the strong confinement regime the exciton behaves similar to the quantum mechanical particle in a box. A smaller box, and thus stronger confinement, leads to splitting of the energy levels (figure 2.3) and increases the bandgap.
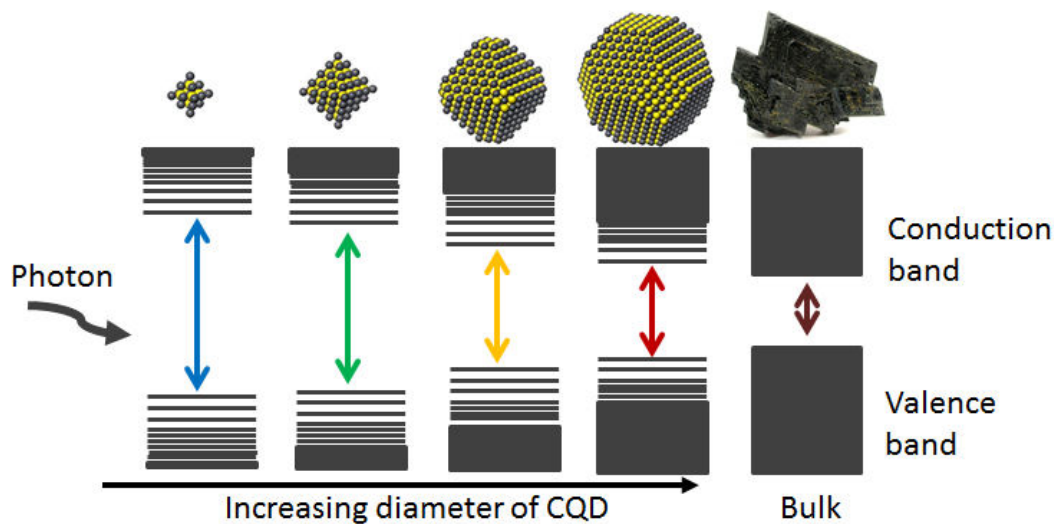
Fig. 2.3 Top: PbS CQDs of increasing diameter, with Pb atoms in black and S atoms in yellow, also bulk PbS on the right. Bottom: schematic of PbS CQDs energy levels. As the PbS CQDs become smaller, their allowed energy levels become more discrete and the bandgap increases. The PbS CQDs absorption starts from photons with higher energy, i.e. shorter wavelength, as the PbS CQDs decrease in size. Figure adapted from Yuan et al.[24] and Choi et al.[31].

For PbS CQDs the electron and hole Bohr radii are $\approx$ 10 nm and the exciton is strongly confined when the PbS CQDs size is decreased beyond these Bohr radii[30]. Current PbS CQD fabrication techniques allow the quantum dot diameter to be easily tuned between 2 to 10 nm. This range in possible CQD diameters and the small PbS bulk bandgap of 0.37 eV provide a large range of PbS CQD bandgaps between 0.6-1.6 eV (see figure 2.4), which makes PbS CQDs an interesting material for solar cells.

Synthesis

PbS CQDs are most commonly synthesized with the hot-injection method. This method allows a quick nucleation of particles followed by a slow growth, which results in monodisperse quantum dots[33]. For PbS quantum dots synthesis, PbO is dissolved in oleic acid (OA) and octadecene (ODE) to create a lead oleate precursor and for the sulfur precursor, bis(tri methylsilyl)sulfide
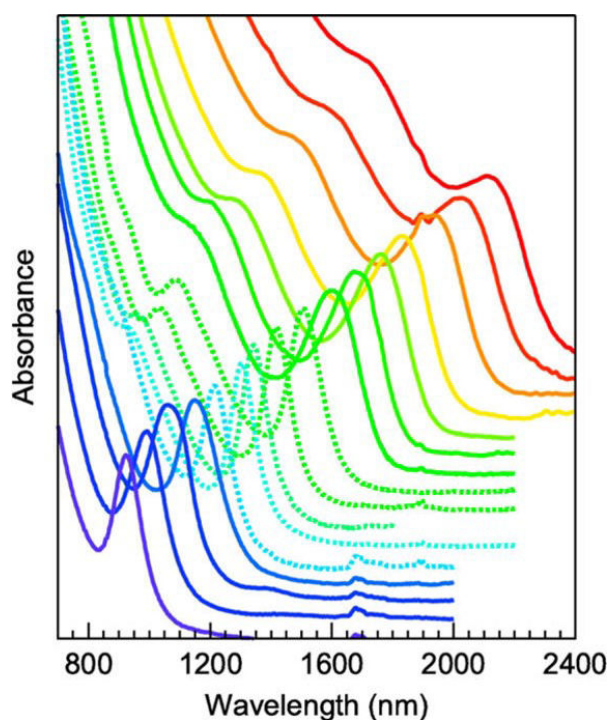
Fig. 2.4 Absorption spectra of solution processed PbS CQDs, demonstrating the large range over which the PbS CQD bandgap can be tuned (absorption spectra are normalized and offset vertically for clarity). Figure taken from Moreels et al.[32].

(TMS) is dissolved in ODE. The sulfur precursor at room temperature is then injected rapidly into a vigorously stirred high temperature lead precursor. This rapid injection results in a supersaturation of the reagents which is relieved by nucleation. The rapid nucleation, of which the rate can be controlled by changing the temperature of the lead precursor and by the degree of supersaturation[7], is followed by the the addition of lead and sulfur monomers to the existing nuclei. Since the lead and sulfur precursors readily react, a stabilizing ligand, such as OA, is added to the solution to prevent bulk particles and control the nucleation and growth rate.

There are multiple routes to control the final size of the CQDs, such as changing the injection temperature, reaction time and the concentration of ligands and reagents.[34]. Increasing the injection temperature results in increased reaction rates and leads to larger CQDs. Whereas reducing the reaction time, for example by adding a cold solvent that quenches the reaction and stops further growth, smaller CQDs can be obtained. Increasing the concentration of OA, increases the solubility of the monomers, which stimulates growth over nucleation, resulting in larger CQDs. By changing these parameters the PbS CQD size can be tuned over a large range in sizes (figure 2.4).

2.2.2   Solar Cell Architectures

The earliest solar cells with CQDs as the the primary active material used a Schottky junction architecture.[35,36]. These Schottky CQD solar cells combined a layer of quantum dots with a transparent conductive oxide, typically ITO, and a reflective metal back contact. The transparent conductive oxide forms an ohmic contact with the CQDs, while the combination of the generally p-type CQDs with shallow work function metal, such as aluminum, creates a rectifying Schottky barrier. This Schottky barrier causes band bending in the CQD layer and results in a depletion region near the interface, which helps separate the charge carriers. However, the performance of the Schottky junction CQD solar cells is limited by a low V_{oc} due to a large barrier height caused by Fermi-level pinning at the interface between the metal and the CQD film[14]. In addition, at the other interface, between the CQD layer and transparent conductive oxide, there is no barrier for the holes as well as no rectification, while much of the light absorption occurs in this area.[23].

An improvement on the Schottky CQD solar cell architecture can be made by adopting a p-n heterojunction architecture[37]. In this architecture an electron accepting n-type semiconductor is combined with a hole accepting p-type semiconductor. For an efficient solar cell these semiconductors should form a type II heterojunction in which conduction- and valance band of the p-type semiconductor have an higher energy than the corresponding n-type bands. This offset in the energy levels provides a built-in potential, which creates a depletion region to separate the charge carriers[38]. In CQD solar cells the generally p-type PbS CQDs are typically combined with n-type metal oxides, such as TiO_2 or ZnO. However, accurate band alignment between the CQDs and the metal oxides is essential for for efficient electron injection into the metal oxide, while minimizing losses to the V_{oc}.[7]

2.3   Valence Band Edge

Precise knowledge of the CQD energy bands is crucial for the engineering of heterojunctions and for accurate device modeling[39]. A standard technique for determining the valence band edge in semiconductors is ultraviolet photoelectron spectroscopy (UPS). By measuring the energy of the electrons that are emitted by the ultraviolet photon a spectrum of the valence band is constructed. The valence band edge is then determined from the energy onset in this spectrum, in comparison to the energy of a metal with a well-known work function. Additionally, the conduction band edge is then often determined by addition of the bandgap energy to the valence band edge.

UPS is often used on CQD films to determine the valence band edge dependence on CQD size, for example by Jasieniak et al.[40] and others[42–44]. Also for PbS CQDs, UPS is the standard
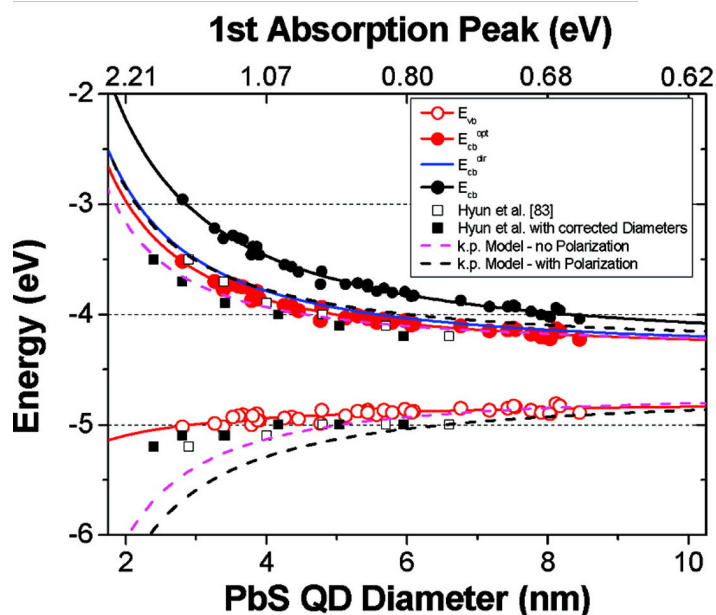
Fig. 2.5 PbS CQD size dependent valence band edge (red circles) and as the corresponding conduction band edge (solid dots) as measured with UPS by Jasieniak et al. [40], including calculations (dashed lines) and cyclic voltammetry measurements on the conduction band by Hyun et al. [41]. Figure taken from Jasieniak et al. [40]

technique for determination of the valence band edge [11,16,40,45–48]. It was found by Jasieniak et al. that for PbS and PbSe CQDs the valence band edge remains changes only marginally with CQD size and thus most of the change occurs in the conduction band (see figure 2.5), while for CdSe and CdTe CQDs the two bands change similarly. This result is unexpected for the PbS and PbSe CQDs since the effective masses of electron and holes are very similar. There is, however, recent discussion on whether the standard UPS analyses used by Jasieniak et al. and others can be accurately applied to lead based semiconductors [49–51], such as PbS CQDs [20,52].

2.3.1 Bilayer PbS CQD:C_{60} Heterojunction Solar Cell

In this work we use a different approach to determine the valence band edge size-dependence of PbS CQD films. This is approach is based on the combination of different bandgap PbS CQD films with organic semiconductor material C_{60} in a bilayer PbS CQD:C_{60} hybrid heterojunction architecture [53] (figure 2.6 a)). PbS CQD films with a large enough bandgap are known to form a type II heterojunction with fullerene derivative C_{60} (Buckminsterfullerene) [54].

This hybrid (organic-inorganic) heterojunction architecture utilizes the n-type C_{60} as an electron acceptor layer which can provide efficient charge carrier separation at the interface, instead of a n-type metal oxide. A solid state CQD ligand exchange with 1,3 benzenedithiol

(BDT) results in a crosslinked p-type PbS CQD film. This combination of a p-type PbS CQD film with n-type C_{60} results in effective blocking of the excitons at the interface and efficient charge extraction. The layer of C_{60} is topped with 1 nm of LiF as a additional hole blocking layer and an reflective aluminum as a top contact[38]. Besides a hole blocking layer, the device also utilizes a layer of MoOx between the PbS CQD film and the transparent conductive oxide ITO, this layer of MoOx is known to effectively block the excitons and provides efficient hole extraction[55].
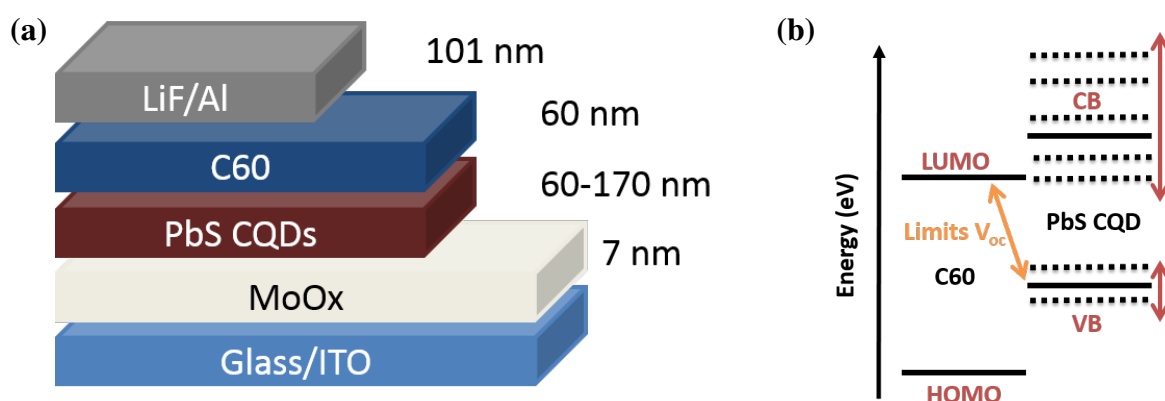
Fig. 2.6 (a) Bilayer heterojunction PbS CQD:C60 solar cell architecture (b) Schematic energy diagram of C60 and PbS CQD, depicting the C60 LUMO and HOMO and the PbS CQD valence- and conduction band edge change as the PbS CQD bandgap changes.

2.3.2   Size-Dependent Open-Circuit Voltage

The bilayer PbS CQD:C_{60} heterojunction solar cell architecture described above allows us to study changes in the optoelectronic properties of the PbS CQDs upon changing the CQD size (i.e. bandgap). The analogue of organic semiconductors to the valence band edge and conduction band edge in inorganic semiconductors are the highest occupied molecular orbital (HOMO) and the lowest unoccupied molecular orbital (LUMO) respectively, with the bandgap determined by the difference between the HOMO and LUMO. The energy levels of these molecular orbitals are discrete, and thus no band bending is expected at the interface of the C_{60} with the PbS CQD film. A consequence of these discrete energy levels is that the difference between the C_{60} LUMO and the PbS CQD valence band edge is well defined.

This difference between the C_{60} LUMO and the PbS CQD valence band edge limits the V_{oc} of the solar cell. The V_{oc} of a solar cell is determined by the quasi-Fermi level difference of the electrons and holes. In Schottky solar cells this difference is limited by the quasi-Fermi level in the semiconductor and the work function of the metal[56]. Whereas in heterojunction solar cells

the V_{oc} is the difference of the quasi-Fermi level of the electrons in the n-type semiconductor and the quasi-Fermi level of the holes in the p-type PbS CQDs. In heterojunction solar cells these quasi-Fermi levels are limited by the diagonal bandgap of the heterojunction, here determined by the PbS CQD valence band edge and the C_{60} LUMO(figure 2.6 b). The optoelectronic properties and energetics of the C60 layer are not altered when changing the PbS CQD size. The size dependence of the V_{oc} in combination with size-dependent recombination measurements, can therefore be used to probe the size dependence of the PbS CQD valence band edge.

Chapter 3

Methods

3.1 Colloidal Quantum Dot Synthesis

The PbS CQDs were synthesized by the hot injection method, developed for PbS CQDs by Hines *et al*,[57] and is mostly based on further developments described in literature[15,16,11].

3.1.1 General

This section describes a typical synthesis. In order to obtain different sized PbS quantum dots, the injection temperature, ratio's of the chemicals and cooling method differ from batch to batch and are described in the next section. All chemicals are purchased from Sigma-Aldrich unless stated otherwise.

In a typical synthesis, the lead precursor was prepared by combining 0.45 g of PbO (99.999%, Alpha Aesar), 14.2 g ODE (technical grade 90%) and 1.34 g of OA (technical grade 90%) in a three-necked Schlenk flask. This mixture was placed under vacuum and heated to 95°C to degas and to form a clear solution. The solution was placed under nitrogen and the temperature was increased to 140°C.

For the sulfur precursor, 0.213 mL of TMS (synthesis grade) was combined with 10 mL of ODE in a glove box and loaded in a 20 mL syringe. The ODE used for the sulfur precursor was degassed and dried by heating to 80°C under vacuum for 18 hours. The Schlenk flask with the lead precursor was transfered to a heating mantle kept at room temperature and allowed to cool to the desired injection temperature T_{inj} before injection of the sulfur precursor. At a temperature T_{inj} of 120°C the sulfur precursor was rapidly injected into the Schlenk flask whilst stirring vigorously. The solution was then allowed to cool to 30-35°C at which point the reaction was quenched with 20 mL of acetone (dried, VWR).

3.1.2   Different CQD Sizes

The synthesis described above was varied to achieve the different PbS CQD sizes (see table 3.1). The techniques used here to vary the CQD size are adapted from methods used in literature[58,34]. For the synthesis of the small bandgap PbS CQDs, 0.7 eV and 0.8 eV, the ratio of OA to ODE was increased. In the lead precursor the OA content was increased to 14 g and the ODE content reduced to 10 g. The amount of ODE in the sulfur precursor was also reduced to 5 mL. Additionally, the reaction solution was kept in the hot heating mantle, which was turned off, resulting in slower cooling. The injection temperature T_{inj} for bandgaps 0.7 eV and 0.8 eV was 150°C and 120°C respectively. For PbS CQDs with bandgaps 1.1 eV, 1.2 eV and 1.3 eV only the injection temperatures were changed with respect to the typical synthesis. The injection temperatures T_{inj} were 180°C, 150°C, 120°C for bandgaps 1.1 eV, 1.2 eV and 1.3 eV respectively. The largest bandgap PbS CQDs, 1.4 eV and 1.5 eV, were synthesized by quenching the reaction shortly after the injection at temperatures T_{inj} of 110°C and 100°C respectively. The quenching was done by rapidly adding 20 mL of cooled hexane (6°C, anhydrous) into the Schlenk flask.

Table 3.1 Overview of synthesis parameters for the different sized CQDs.

| Bandgap (eV) | Lead precursor | | Sulfur precursor | Heating | | |
	ODE (g)	OA (g)	ODE (mL)	T_{inj} (°C)	Hexane	Mantle swap
0.7	10	14	5	150	no	no
0.8	10	14	5	120	no	no
1.1	14.2	1.34	10	180	no	yes
1.2	14.2	1.34	10	150	no	yes
1.3	14.2	1.34	10	120	no	yes
1.4	14.2	1.34	10	110	yes	yes
1.5	14.2	1.34	10	100	yes	yes

3.1.3   Solution Based I$_2$ Passivation

The procedure of the solution-based I_2 treatment described here is similar to the process described in Lan *et al*[10]. After the synthesis, the CQDs were transferred into a glovebox (<0.5 ppm O_2, <0.5 ppm H_2O) and precipitated with additional acetone. The quantum dots were then centrifuged for 4-10 minutes at 4000-5000 rpm and the supernatant was discarded. This was followed by drying the CQDs in vacuum overnight. After full drying, the CQDs were weighed and dispersed in toluene ($\geq$ 99.9%) at a concentration of 150 mg/mL. For the passivation, iodine (99.999%) was dissolved in toluene at a concentration of 25×10^{-3} M and added to

the CQD solution in a ratio of 1:5. The solution was then stirred for 24 hours after which the quantum dots were precipitated with methanol and centrifuged for 2-5 minutes at 1500-5000 rpm. Again, the supernatant was discarded and the CQDs were dried in vacuum overnight. Finally the CQDs were dispersed in octane (37.5 mg/mL).

3.1.4 UV/Vis

Absorption spectra were measured with a Perkin Elmer LAMBDA 750 UV/Vis/NIR spectrometer on a solution of CQDs in octane using a quartz cuvette. Figure 3.1 shows the absorption spectra of the different sized PbS CQDs (see Methods 3.1.2). PbS CQDs start absorbing when the photon energy is large enough to excite the first electronic state. This results in the peaks seen in the absorption spectra and the width of these peaks is caused by the PbS CQD size distribution. The PbS CQD bandgap is determined as the maximum of the first absorption peak.
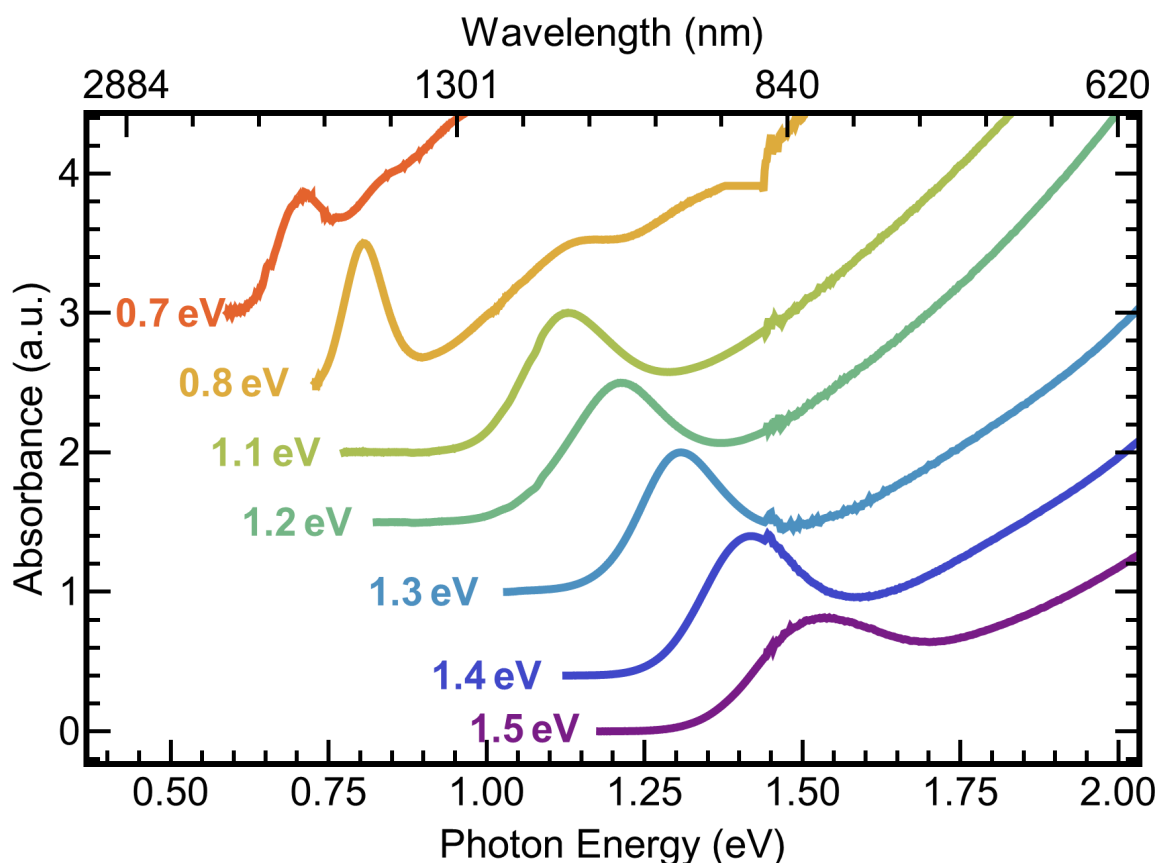
Fig. 3.1 Normalized and vertically shifted absorbance spectra of different sized CQDs. Note that the noisy signal around 860 nm and 1720 nm is due to measurement artifacts and not due to CQD absorbance.

3.2   Solar Cell Fabrication

3.2.1   Substrate Cleaning

Patterned ITO coated glass substrates (15 mm x 15 mm, $22\Omega/\square$, Kintec) were cleaned with a toothbrush and a soapy solution ("micro-90 concentrated cleaning solution" in distilled water) followed by a 15 minute sonication in an ultrasonic bath. The substrates were then rinsed with deionized water and sonicated in deionized water, acetone and isopropanol for 15 minutes each. After sonication in isopropanol, the substrates were placed in an oven to dry. When dry, the substrates were oxygen plasma cleaned for 15 minutes (Diener electronic Zepto plasma system).

3.2.2   Thermal Evaporation

The cleaned substrates were transferred into a glove box (<0.1 ppm O_2, <0.2 ppm H_2O) for deposition of the different layers. Before spin coating of the CQD layer, a hole-blocking layer of 7 nm MoOx (99.97%, Aldrich) was deposited by thermal evaporation (Angstrom Engineering Amod) under vacuum at a rate of 0.5 Å/s and a pressure of 8×10^{-7} Torr. After spin coating of the CQD layer, a 60 nm layer of electron acceptor material fullerene-C_{60} (99.9%, Aldrich) was deposited by evaporation under similar vacuum conditions at a rate of 1 Å/s. Finally, 1 nm of LiF (99.995%, Aldrich) and 100 nm of Al (99.999%, Kurt J. Lesker) were deposited successively at a rate of 0.35 Å/s and 1 Å/s respectively. The LiF/Al top contact was deposited through a shadow mask, resulting in eight separate and different-sized solar cells on each device (figure 3.2) .
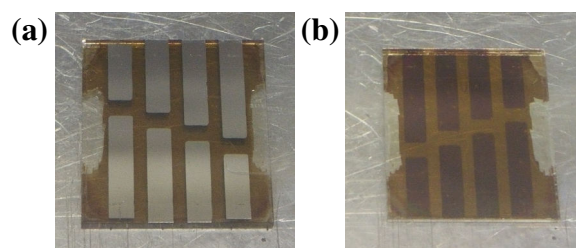
Fig. 3.2 (a) Photograph of the device after evaporation of the LiF/Al contact through a shadow mask showing the eight individual solar cells. (b) The same device photographed from the glass side (note: scratched transparent part on the sides of the device is prepared to contact the ITO layer.

3.2.3   Spin Coating

CQDs were deposited on the substrate by layer-by-layer spin coating under inert conditions. Each of the five CQD layers were crosslinked by 1,3-benzenedithiol (99%,) and the remaining ligands were washed away with acetonitrile (anhydrous). First, two drops of CQDs in octane (37.5 mg/mL) were deposited on the substrate with a 5 mL syringe through a 0.2 μm PTFE membrane filter, followed by spin coating. In the following step, a solution of 1,3-benzenedithiol in acetonitrile (0.1% v:v) was deposited on the substrate and spun after soaking for 30 seconds. The substrate was then soaked in acetonitrile and spun to wash away remaining ligands. This last washing step was repeated three times and followed by the deposition of CQDs for the next layer. All of the above spin coating processes are realized by spinning at 2500 rpm for 10 seconds with a SCS G3 Spin Coater.

3.3   Solar Cell Characterization

3.3.1   Current-Voltage Characteristics

Current-Voltage characteristics were measured under 1 sun illumination provided by a Newport Oriel Sol2a Solar Simulator. Before each measurement the intensity of the xenon lamp was calibrated with a Newport Oriel 91150V crystalline silicon reference Cell. A device with solar cells was taken from the glovebox in a closed and transparent sample holder and measured with a Keithley 2401 SMU after 5 minutes of light soaking under 1 sun illumination. In order to filter out the shorted or pinhole-rich solar cells only the solar cells with an efficiency of at least half the maximum efficiency of the solar cells on each device are taken into account (see table 3.2).

Table 3.2 Number of solar cells for each bandgap with an efficiency $\eta > \frac{1}{2}\eta_{\max}$

Bandgap	#
0.7 eV	5/8
0.8 eV	12/16
1.1 eV	7/16
1.2 eV	12/16
1.3 eV	15/16
1.4 eV	11/16
1.5 eV	9/16

3.3.2   Transient Photovoltage Measurements

Transient photovoltage (TPV) measurements were performed to characterize the voltage decay times of the most efficient solar cell on each device for CQD bandgaps of 0.8 eV or higher. A Thorlabs cold white collimated LED was used as a light bias to illuminate the sample with different intensities (0.025, 0.05, 0.10 and 0.20 sun). This light bias was focused on the sample with two lenses. The intensity of this light bias was calibrated before each measurement with a Newport Oriel 91150V crystalline silicon reference cell. The sample was then illuminated with a pulsed signal from a 525 nm LED. A function generator (RIGOL DG1062) was used to actuate the LED with a voltage of 10 V and a frequency between 60 Hz and 9 kHz, depending on the sample and applied light bias. The voltage transients were measured using a Picoscope 6402 C oscilloscope with an impedance of 1 MΩ (figure 3.3).
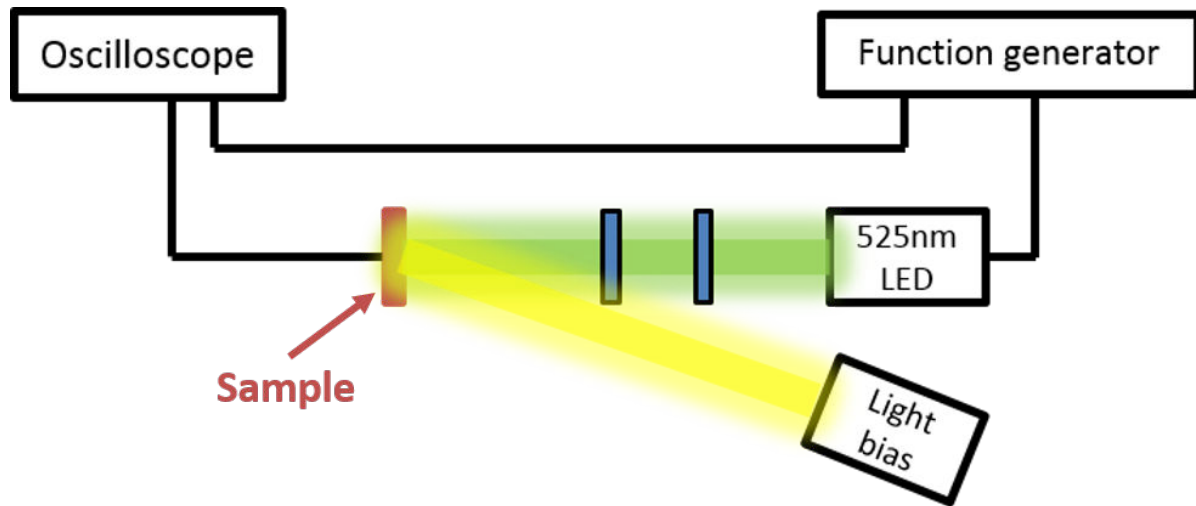
Fig. 3.3 Transient photovoltage setup

The TPV measurements were performed under open circuit conditions, since no almost current is extracted from the sample due to the high impedance oscilloscope. This means that the charges generated by the constant light bias and the pulsed LED pulse cannot be extracted through the contacts. The constant light bias then generates charges which results in a baseline open-circuit voltage (V_{oc}). This V_{oc} is increased by ΔV_{oc} as the pulsed LED illuminates the sample and generates more charges. These charges can not escape through the contacts either, however charges can decay through recombination. Turning off the LED results in exponential decay of ΔV_{oc} due to charges recombining and the voltage returns to ΔV_{oc} (see figure 3.4)[59]. This transient of the voltage can then be fitted to extract the decay time τ.
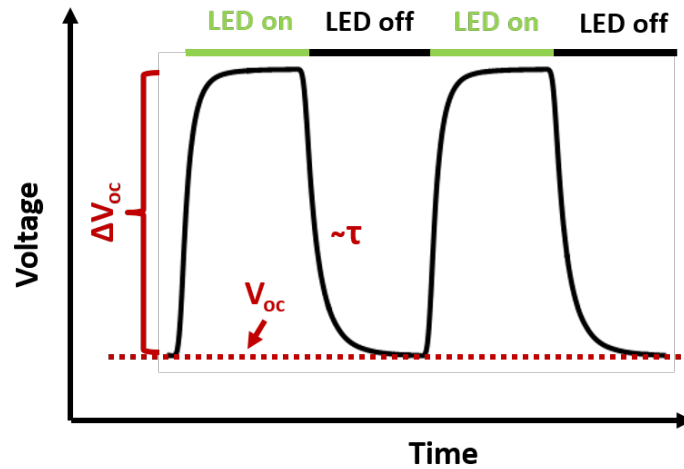
Fig. 3.4 Schematic representation of a TPV measurement, showing the baseline open circuit voltage V_{oc} generated by the light bias, the additional voltage ΔV_{oc} generated by the pulsed LED and the voltage decay with decay time τ after the LED is turned off

Requirements for whether the voltage transient was fitted with a single or with a double exponential decay were as follows: if the amplitude of the second exponential was larger than 1/10 of the first exponential and the decay time was at least a factor of 2 different than a double exponential was used, if not, than a single exponential was used to describe the transient. For the comparison of decay times only the fast decay was taken into account, since the fast decay component was dominant for all measurements (see figure 4.4).

3.3.3   Atomic Force Microscopy

Atomic Force Microscopy was performed with a Veeco Dimension 3100 AFM using a NT-MDT NSG01 gold coated silicon tip in tapping mode. In order to determine the height of the CQD film devices were prepared with-out the C_{60} layer and the LiF/Al top contact. A metallic tweezer was used to make a scratch on the CQD films. AFM was then used to scan a height profile of the scratch. The difference between peaks of height distribution profiles of the AFM image around the scratch was used to determine the thickness of the CQD film. Analysis of the AFM images was done with Gwyddion software.

3.3.4   External Quantum Efficiency

External quantum efficiency (EQE), i.e. the ratio of extracted electrons to the number of incoming photons per wavelength, was measured with a Newport Oriel QUANTX 300. This system has an integrated light source, beam chopper with virtual digital lock-in amplifier and

uses a monochromator with an automated filter selection to scan different wavelengths. The system was calibrated with a silicon solar cell before each measurement.

Chapter 4

Results and Discussion

In this chapter the PbS CQD:C60 bilayer heterojunction solar cells made with different sized PbS CQDs are characterized and compared with literature. First, PbS CQD films are measured with AFM to determine the thickness of the layer we are interested in. Second, the performance of PbS CQD solar cells made with different sized PbS CQDs is characterized and the performance of the solar cells is compared. Third, the effect of recombination on the open-circuit voltage (V_{oc}) is studied by measuring photovoltage decay times with transient photovoltage (TPV) measurements. Finally, the results of the measured PbS CQD size-dependent V_{oc} and photovoltage decay times of the solar cells are compared with literature on measurements and calculations performed on the PbS CQD size-dependent valence band edge energy.

4.1   Film Thickness

Before comparison of the optoelectronic properties of the solar cells investigated here, we first look at the film uniformity of the solar cells fabricated from different sized CQDs. The variations in the thermally evaporated layers (MoOx, C_{60}, LiF and Al) are assumed to be negligible for the solar cells with different sized PbS CQDs, since the deposition for each of these layers happens simultaneously. However, variations in the PbS CQD film can arise during the deposition by spin coating. Even though the spin coating of the PbS CQD films happens in the same inert environment and the same solvents, there can be small variations in soaking time, drop-casted volume, and PbS CQD concentration.

The thickness of the CQD films was measured with AFM (see Methods 3.3.3) on scratched PbS CQD films. From the results of the measurement shown in table 4.1 it can be seen that the film thicknesses vary between 60 nm and 170 nm. However, the variation for films of PbS CQD with bandgaps 1.1-1.4 eV is only around 10 nm. The largest difference in film thickness is found for the small bandgap PbS CQDs of 0.7 and 0.8 eV, with both a thickness below 100 nm.

Table 4.1 CQD film thickness for PbS CQDs with different bandgaps

Bandgap	Film thickness (nm)
0.7 eV	92 ± 17
0.8 eV	60 ± 7
1.1 eV	142 ± 9
1.2 eV	149 ± 18
1.3 eV	153 ± 6
1.4 eV	144 ± 9
1.5 eV	178 ± 20

Especially, the 0.8 eV CQD film with a thickness of 60 nm differs significantly from the other devices. Most likely, this is due to a relatively low concentration of PbS CQDs in octane for the CQDs with bandgaps 0.7 eV and 0.8 eV. The PbS CQD films were fabricated and measured several months after fabrication of the solar cells and, although, solar cells made with these films are also more transparent to the eye, some of the difference might be due aggregation of the large 0.7 eV and 0.8 eV PbS CQDs. This aggregation could reduce the concentration of PbS CQDs in the drop-casted solution on the device before spin coating. Also, it was noted for the 0.7 eV CQDs that the PTFE filter was clogged after deposition of the CQD layers.

4.2 Solar Cell Performance

The performance of the solar cells with different bandgap PbS CQDs is determined from J-V characteristics (see Methods 3.3.1). First, we compare the J-V curves of the most efficient solar cell for each of the different PbS CQD bandgaps in Figure 4.1. It shows that the most efficient solar cell made from PbS CQDs with a bandgap of 0.7 eV has a very low efficiency (η) of 0.06%, resulting from a low current density (J_{sc}), a low fill factor (FF) and a low open-circuit voltage V_{oc} when compared with the other bandgaps. This relatively low efficiency of the 0.7eV bandgap solar cell, in combination with the s-shaped J-V curve, indicates that there is a energy barrier for the charges[16,60,61]. The 0.7 eV Pbs CQD film likely no longer forms a type II heterojunction with the C_{60}. Instead there is a type I heterojunction[54] in which the C_{60} LUMO is higher in energy then the PbS CQD conduction band edge (see figure 2.6). For the most efficient 0.8 eV PbS bandgap solar cell there is a small dent in the J-V curve, which means that there might also be a small barrier present. However, the overall performance of the 0.8 eV bandgap PbS CQDs is strongly improved when compared with 0.7 eV bandgap PbS CQDs. Also, the J-V curves of the best solar cells for the other PbS CQD bandgaps show a significantly better performance. Larger bandgaps show a strongly improved J_{sc}, with the

exception of the best solar cell of 1.1 eV bandgap PbS CQDs. The 1.1 eV bandgap solar cell also shows a relatively low FF, but the V_{oc} has significantly improved compared to the smaller bandgaps. A further increase of the PbS CQD bandgap results in a further increase of the V_{oc}, as can be seen from the J-V curves.
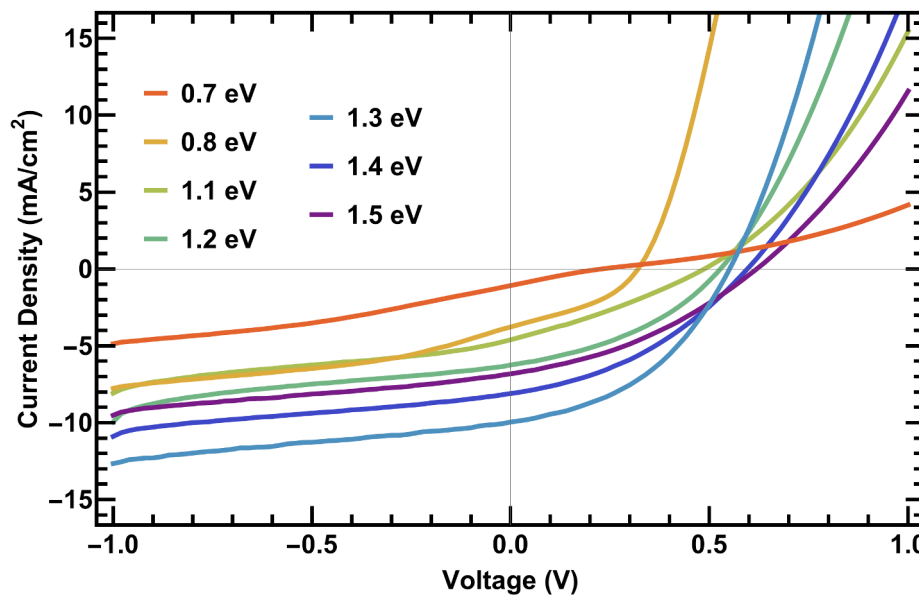
Fig. 4.1 J-V curves of the most best efficient solar cell from each of the different PbS CQD bandgaps.

Now, we compare the J-V parameters of multiple solar cells made from each of the PbS CQDs bandgaps, shown in figure 4.2. The efficiency of the solar cells varies from about 0.5% for 1.1 eV PbS CQDs to 2.3% for 1.3 eV PbS CQDs, which is mostly from variations in J_{sc}. The solar cells made with 0.7 eV PbS CQDs have an extremely low efficiency which, as indicated by the s-shaped J-V curve, is likely an result of unfavorable energetics at the boundary of C_{60} with the PbS CQD film.

Besides variations in J_{sc} between the different bandgaps, there are also variations in the J_{sc} and thus the efficiency of solar cells from the same bandgap. J_{sc} is strongly depended on the fabrication quality of the the solar cell layers. The PbS CQD solar cells suffer from pinholes that originate from the PbS CQD spin coating and can result in severe losses of J_{sc}. Furthermore, the J_{sc} depends on the thickness of the PbS CQD layer, which varies between the CQD bandgaps (see section 4.1) and can also vary slightly between solar cells made with the same bandgap PbS CQDs. For 1.1 eV PbS CQD solar cells it is likely that pinholes have led to the low J_{sc} and efficiency. Less than half of these solar cells had an efficiency comparable with the best and many solar cells were shorted (see section 3.3.1). As for the 0.8 ev PbS CQD solar

cells, the relatively thin PbS CQD film thickness (see 4.1) reduces absorption and results in lower efficiency.

The J_{sc} of PbS CQD solar cells with the same bandgap varies strongly, which could be due to variations in the fabrication quality. V_{oc} on the other hand, mostly depends on the solar cell architecture and the optoelectronic properties of the materials. From figure 4.2 it can be seen the V_{oc} of solar cells with the same bandgap PbS CQDs varies only marginally. However, there appears to be a strong dependence of the V_{oc} with PbS CQD bandgap, varying over many standard deviations between 0.8 eV and 1.5 eV. Whereas the variations in FF and J_{sc} with PbS CQD bandgap are much smaller compared to their standard deviations. Even though the solar cell performances varies between cells, the V_{oc} of these solar cells can still be utilized as a measure for the optoelectronic properties of the materials in the solar cells. Which means that the V_{oc} can be used an indication of the optoelectronic properties of the PbS CQDs, since the PbS CQDs film is the only layer that is varied between the solar cells.
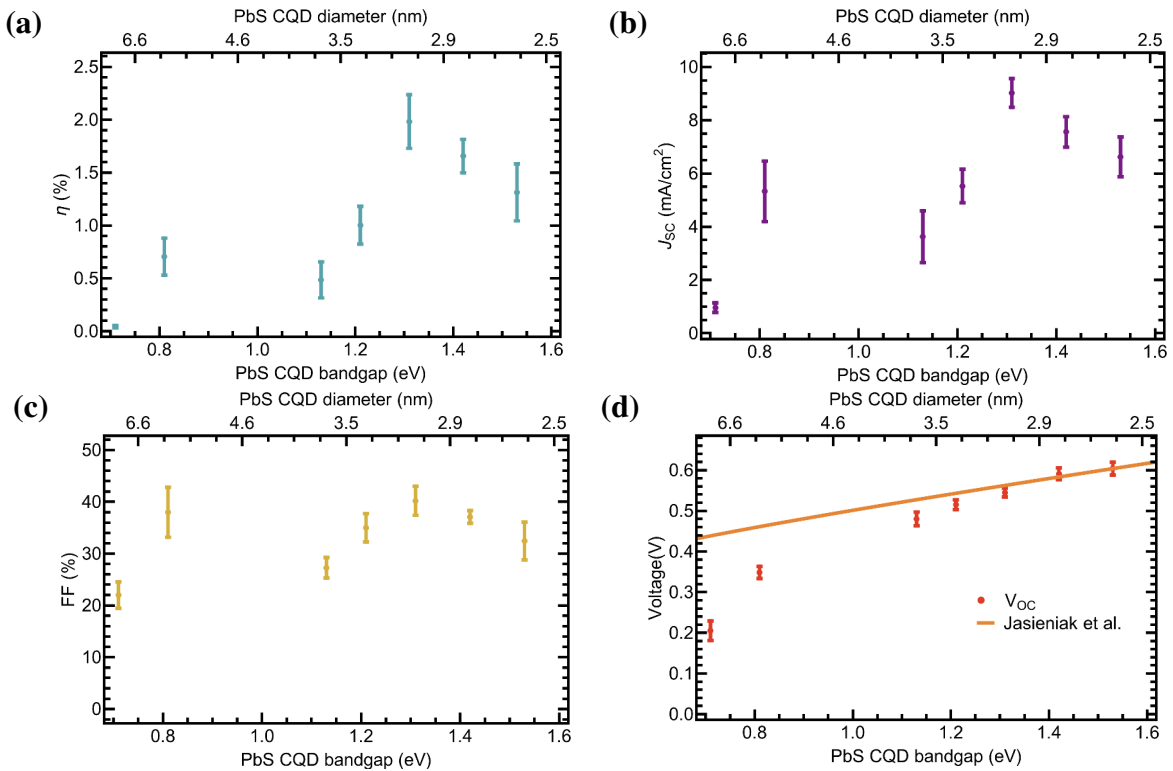

Fig. 4.2 Solar cell performance parameters from J-V measurements. (a) Average efficiency of the solar cells for each of the PbS CQD bandgaps, (b) average short-circuit current density J_{sc}, (c) average fill factor FF and (d) average open-circuit voltage V_{oc} with the predicted change in V_{oc} from the change in valence band energy as measured by Jasieniak et al.[40].

Open-Circuit Voltage

The V_{oc} of solar cells depends on the difference in energy between the quasi-Fermi levels of the electrons and holes[62–64]. In the bilayer heterojunction solar cells studied here this difference in energy is limited by the diagonal bandgap, i.e. the difference of the C_{60} LUMO and the PbS CQD valence band. A change in V_{oc} with bandgap could be explained from a change in PbS CQD valence band, because the C_{60} LUMO energy is fixed. This change in valence band energy of PbS CQDs, measured with photoelectron spectroscopy by Jasieniak et al.[40], is compared in figure 4.2 with the measured change in V_{oc} of the bilayer heterojunction solar cells. The expected change in V_{oc} from the measured change PbS CQD valence band does show a similar trend as the measured V_{oc}. However, the measured change in V_{oc} with bandgap is significantly larger than the predicted change in V_{oc} from the PbS CQD valence band energy change measured by photoelectron spectroscopy. In the following sections this discrepancy will be investigated.

4.2.1 External Quantum Efficiency

In addition to J-V measurements, we performed external quantum efficiency (EQE) measurements on solar cells made of PbS CQDs with bandgaps 1.3 eV, 1.4 eV and 1.5 eV. Figure 4.3 shows the EQE spectra of these solar cells and the corresponding J-V curves. The increase in short-circuit current J_{sc} for these solar cells as the bandgap decreases is in part due to increased absorption in the longer wavelength range, which is to be expected for smaller bandgap PbS CQDs. Multiplying the photon flux of the solar spectrum with the EQE for each wavelength and integrating over all wavelengths, following equation 4.1, is another method to determine J_{sc}.

$$J_{sc} = q \int_{0}^{\lambda_{max}} \Phi(\lambda) \cdot EQE(\lambda) \cdot d\lambda \tag{4.1}$$

Table 4.2 shows a comparison of J_{sc} calculated from EQE measurements and J_{sc} from J-V measurements, the good resemblance between the two indicates that the J-V measurements are an adequate probe for the solar cell performance.

4.3 Recombination

The V_{oc} of heterojunction solar cells does not only depend on the diagonal band gap (figure 2.6 b), here the energy difference between the CQD valence band and the C_{60} LUMO, but also
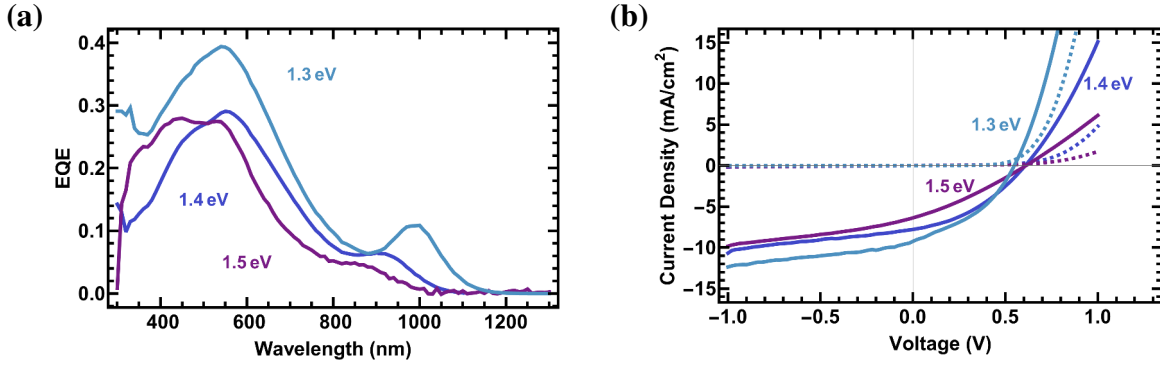
(a)

(b)

Fig. 4.3 Comparison of J-V curves and EQE measurements of single solar cells. (b) EQE of solar cells made with PbS CQDs of bandgap 1.3 eV, 1.4 eV and 1.5 eV. (a) J-V curves of the same solar cells under 1 sun illumination (solid lines) and in the dark (dashed lines).

Table 4.2 J_{sc} comparison from EQE and J-V measurement

Bandgap	J_{sc} from J-V measurement	J_{sc} from EQE
1.3 eV	10.1 mA/cm^2	8.9 mA/cm^2
1.4 eV	6.1 mA/cm^2	6.3 mA/cm^2
1.5 eV	5.8 mA/cm^2	5.4 mA/cm^2

on recombination. An increase in recombination for increased CQD size causes a stronger decrease in the measured V_{oc} with an increase in CQD size than is expected for the change in the diagonal band gap. This increase in recombination with size could be from a change in facets on the CQD surface as the CQDs grow in size. As small CQDs grow in size the non polar (100) facets start to dominate over the Pb-rich (111) facets[31,65]. The (100) facets could be more susceptible to surface oxidation, resulting in surface traps that increase recombination[66].

From equation 2.5 we know that the V_{oc} depends logarithmically on the ratio of illumination current density J_L and dark saturation current density J_0, and the latter is a measure of the recombination. To understand how a change in recombination between the different solar cells would affect the V_{oc}, we subtract the equations for the V_{oc} for devices 1 and 2. This to leads equation 4.2, were we made the assumption that both devices have the same ideality factor n.

The difference in V_{oc} (ΔV_{oc}) depends logarithmically on the ratio of the dark saturation current densities and the light generated current densities. This allows us to predict ratio of recombination rates needed to explain the large difference in V_{oc} measured. The average difference in V_{oc} of solar cells made with 1.5 eV and 0.8 eV bandgap CQDs minus the change in valence band energy from Jasieniak et al. is 113 meV. From equation 4.2 then follows, under the assumption that light generated current density of these solar cell is the same (see figure 4.2), that the ratio of dark saturation current densities $\frac{J_{0,1}}{J_{0,2}} = 78$. Therefore, to account for the

difference in V_{oc} between 1.5 eV and 0.8 eV bandgap CQDs solar cells, the recombination of the latter has to be a factor of 78 larger.

$$\Delta V_{oc} = \frac{nkT}{q} ln(\frac{J_{0,1}}{J_{0,2}} \frac{J_{sc,2}}{J_{sc,1}})$$ (4.2)

4.3.1   Transient Photovoltage

We can study the recombination in the solar cells with different bandgap CQDs with transient photovoltage (TPV) measurements (see Methods 3.3.2). In TPV measurements, a solar cell under open-circuit conditions is perturbed with a short light pulse which generates charges and thus voltage across the solar cell. In a solar cell under open-circuit conditions the charges are not extracted, but the voltage after the light pulse still decays due to recombination. Here, we measure the the decay of this voltage as a function of light intensity provided by a light bias of 0.025-0.200 sun, where 1 sun is defined as 1000 W/m^2. The decay time τ, which is inversely proportional to the recombination rate in the solar cell, is extracted by fitting a single or double exponential function to the voltage decay (see Methods 3.3.2)[59]. In figure 4.4 the single and double exponential fits are shown for the different bandgap CQDs.

Figure 4.5 shows the charge carrier decay times under 1 sun illumination for each of the different bandgaps. From this we find that the decay times, and thus the recombination rates, of all the different bandgaps are comparable. In fact, the average of the decay times differs by only a factor of 5 between the largest bandgap CQDs and the smallest bandgap CQDs. Moreover, the solar cells with 0.8 eV bandgap CQDs have a longer decay time, and thus slower recombination than the solar cells with 1.5 eV bandgap CQDs. This opposite trend means that the stronger decrease in measured V_{oc} with decreasing bandgap cannot be explained by a change in recombination among the different bandgap CQDs.

4.4   Size Dependence of the Valence Band

In the previous sections we found that the dependence of the V_{oc} with PbS CQD bandgap in the bilayer heterojunction solar cells is stronger than predicted from the change in valence band edge measured with photoelectron spectroscopy and that this stronger dependence cannot be explained by a change in recombination. However, recent studies cast doubt on the ability of UPS/XPS to accurately determine the PbS CQD valence band edge. Miller et al.[20] argue that the standard analysis used by XPS and UPS measurements leads to unrealistic values of the valence band edge in PbS CQD. This inaccuracy is caused by a long, low-intensity tail of the density of states (DOS) at the valence band edge. Standard analysis of UPS and
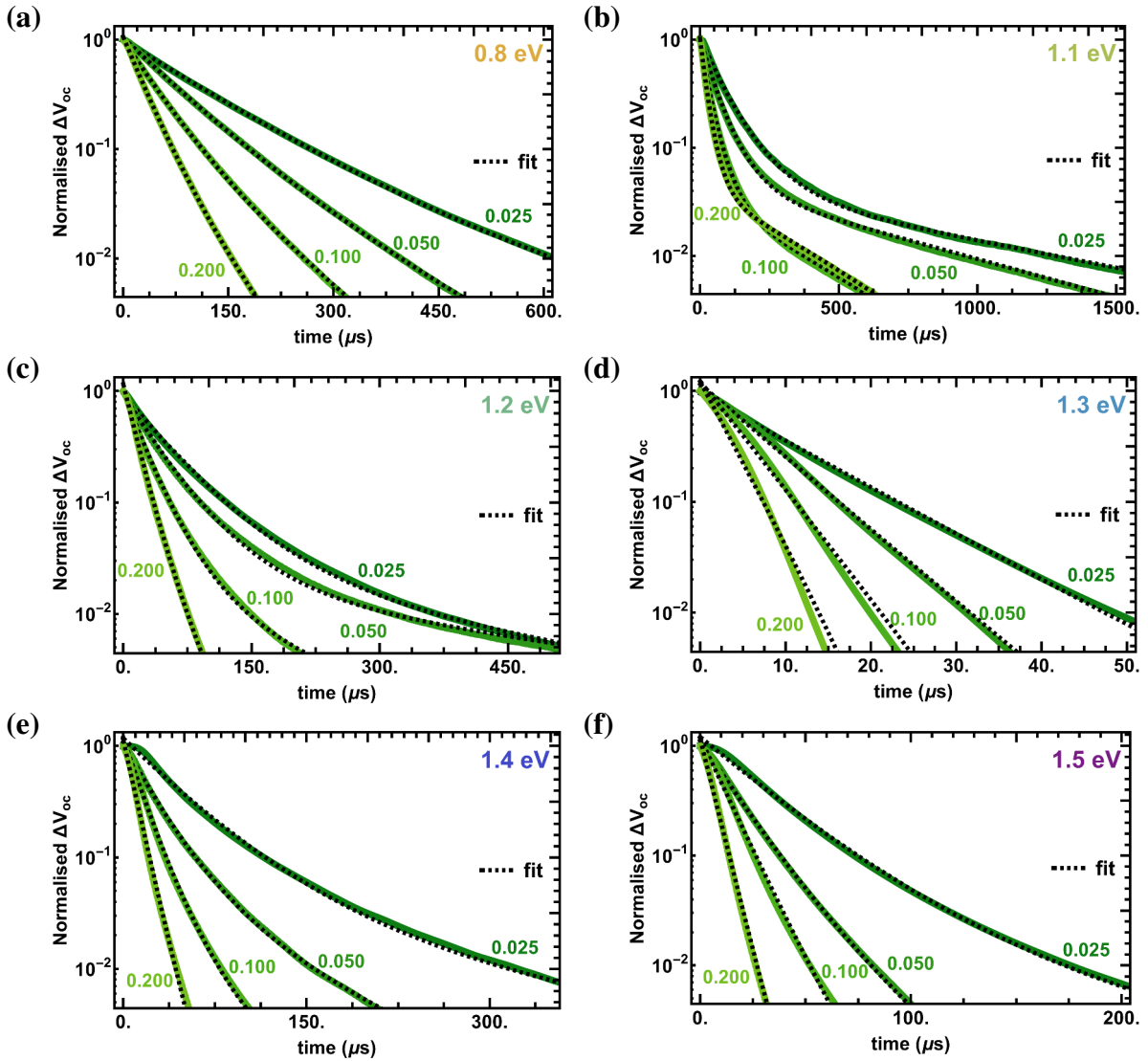
Fig. 4.4 Examples of normalized voltage transients for different light bias intensities: 0.025 sun, 0.050 sun, 0.100 sun and 0.200 sun (black to orange). Also shown are the single or double exponential fits to the voltage transients. Transients and fits of solar cells with PbS CQD bandgaps 0.8 ev, 1.1 eV, 1.2 eV, 1.3 eV, 1.4 eV and 1.5 eV in (a-f).

XPS approximates the valence band edge by a linear extrapolation of the leading edge in the photoemission onset. This analyses to determine the valence band edge from UPS/XPS does not take the low-intensity DOS tail into account.

4.4.1   Correction to Standard Analyses

To determine the origin of this low-intensity tail, Miller et al. compare the GW calculated band structure with the projected DOS of bulk PbS. This comparison shows that the strong increase
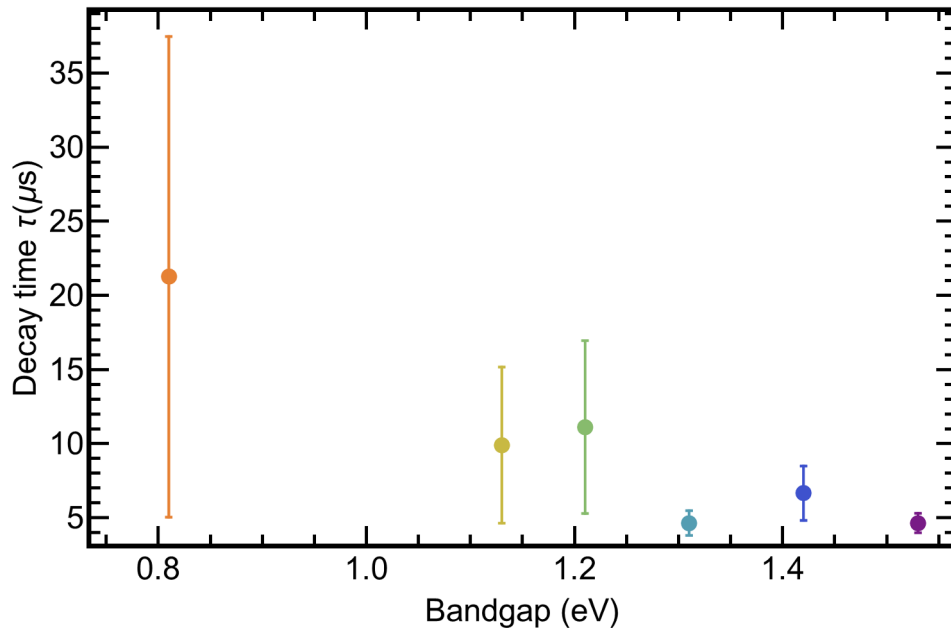
Fig. 4.5 Charge carrier decay times at 1 sun illumination from TPV measurements of different solar cells made with different PbS CQD bandgaps. Plotted decay times are extrapolated to 1 sun from exponential fit to measured decay times at 0.025, 0.050, 0.100 and 0.200 sun. Error bars show one standard deviation confidence bands of fit extrapolated to 1 sun.

in DOS, i.e. the leading edge of the photoemission, comes from the Σ point, whereas the valence band edge at the L point only has a small contribution to the DOS at the valence band edge. It is this small contribution to the DOS from the L point that leads to the low-intensity tail in the photoemission. Instead of a linear extrapolation of the leading edge to determine the valence band edge they use a fitting method similar to that of Kraut et al.[67]. In this method the valence band edge is determined by fitting a parabolic DOS model to the leading edge of the bulk PbS XPS spectrum[20,51].

However, for PbS CQDs the difference between the L point and the Σ point ($L-\Sigma$) decreases as the PbS CQDs decrease in size. This size-dependent $L-\Sigma$ difference is approximated by $k \cdot p$ theory and used in the parabolic DOS model to fit the XPS spectra of the PbS CQD films[30]. From comparison of the valence band edge position determined by this method with the valence band edge position determined by linear extrapolation of the leading edge of the XPS spectrum a linear correction as a function of CQD bandgap is determined: $0.382 - 0.226E_g$. Miller et al. find that linear extrapolation of the leading edge for UPS or XPS gives the same result and therefore apply the correction term (acquired from the model and XPS measurements) to both UPS and XPS results.

In order to compare the corrected XPS and UPS valence band edge with our results we first convert the bandgap E_g used by Miller et al. to the optical bandgap of the CQDs in solution ($E_{opt, sol}$) used as the 'bandgap' in this work. E_g is defined as $E_g = E_{opt, film} + XBE$, where $E_{opt, film}$ is the position of the first exciton peak of the PbS CQD film absorption and XBE is the exciton binding energy. The XBE is then calculated from[47]:

$$XBE = 1.786 \frac{e^2}{4\pi\varepsilon_0\varepsilon_{QD}R} \qquad (4.3)$$

with the elementary charge e, vacuum permittivity ε_0, optical dielectric constant of PbS ε_{QD} and CQD radius R, where the latter is calculated from the first excitonic peak of the PbS CQD absorption in film and a standard sizing curve[68]. From the above we can obtain $E_{opt, film}$, which we then relate to $E_{opt, sol}$ by using the relation between these two as measured by Miller et al.: $E_{opt, film} = 0.98 E_{opt, sol} - 0.01$. The resulting values of the valence band edge, including the correction term, are shown with respect to the Fermi level in figure 4.6. We then fit the data, analogous to the fit by Jasieniak et al., with a function of the form: $a + bx^{-d}$. The result of this fit is also shown in figure 4.6.
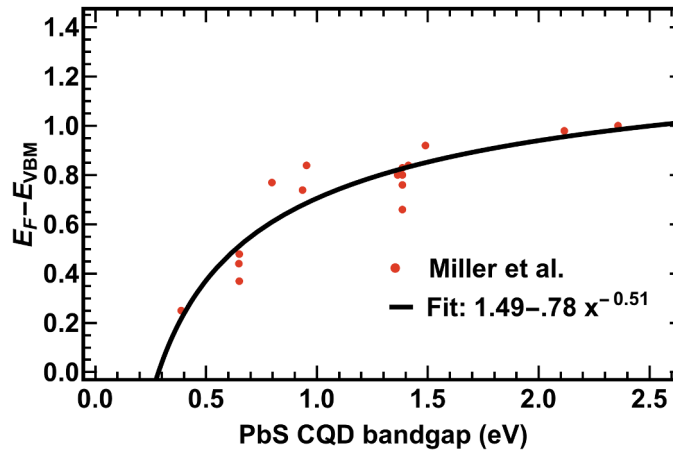
Fig. 4.6 Red: data from Miller et al. of the valence band edge (E_{VBM}) with respect to the Fermi level (E_F) as a function of the PbS CQD bandgap calculated from the first excitonic absorption peak of PbS CQDs in solution. Black: Fit of the form $a + bx^{-d}$ to the data by Miller et al..

4.4.2 Comparison with Measured V$_{oc}$

Before we make a new comparison between the change in the valence band edge and the measured V_{oc}, we first approximate the contribution of the recombination and the differences in J_{sc} on the V_{oc}. The ratio of the decay times τ and the ratio of the J_{sc} of the different bandgap

PbS CQDs is taken with respect to 1.5 eV bandgap PbS CQDs. These ratios are then used in combination with equation 4.2 to determine a correction to the V_{oc}, in order to isolate the effect of the valence band edge change.
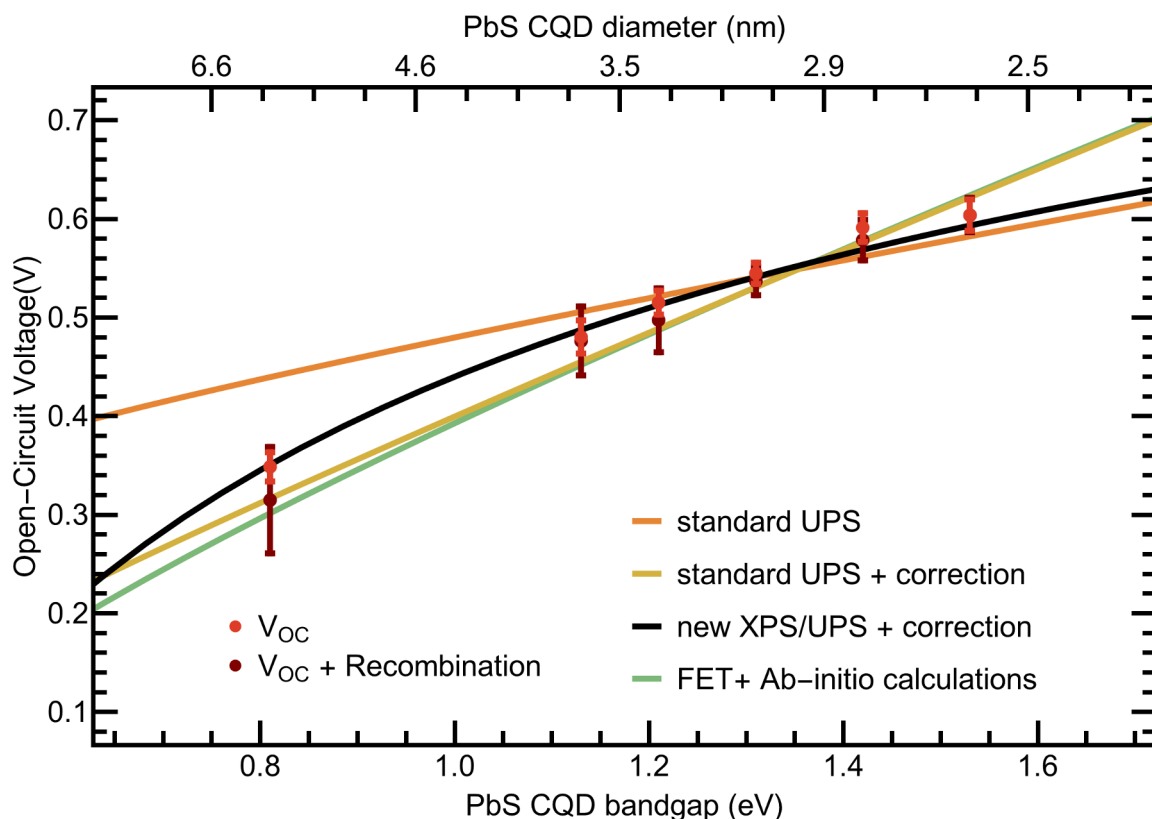
Fig. 4.7 Comparison of the measured V_{oc} and recombination corrected V_{oc} (V_{oc} + Recombination) with expected change in V_{oc} from the change in valence band edge with PbS CQD size. The measured V_{oc} is compared with: standard UPS measurement from Jasieniak et al.[40], UPS results from Jasieniak et al. including the correction term proposed by Miller et al.[20], XPS/UPS measurements by Miller et al. including their correction term and finally field effect transistor (FET) measurements including ab-initio calculations from Bisri et al.[69].

Figure 4.7 shows a comparison of this corrected V_{oc} (shown as 'V_{oc} + Recombination') with the the predicted V_{oc} change from the change in the valence band edge from the measurements and correction by Miller et al.('new XPS/UPS + correction' in figure 4.7). The predicted V_{oc} change from the valence band edge measurements by Jasieniak et al. using the standard UPS analyses is also shown ('standard UPS'), as well as the measurements by Jasieniak et al. with the correction term from Miller et al.('standard UPS + correction'). Additionally, Bisri et al.[69] determined the valence band edge level of PbS CQD films from a combination of experimental data on electric-double-layer-gated transistors and ab-initio theory. The predicted V_{oc} change from their results of the PbS CQD size dependent valence band edge is also shown ('FET +

Ab-initio calculations'). However, it must by noted that their fit for the valence band edge size dependence is performed on data of PbS CQDs with a bandgap of 2 eV and higher.

In order to compare the different predictions for the V_{oc} change, they are offset by fitting the curves of the predicted change in V_{oc} to maximize overlap with the corrected V_{oc} ('V_{oc} + Recombination'). The result of this procedure shows that for all V_{oc} change predictions there is good overlap with the measured V_{oc}, with the exception of predicted V_{oc} change by Jasieniak et al. from valence band edge measurements by UPS. This indicates that due to the low-intensity tail of the DOS in PbS CQDs there is indeed an inaccuracy in the standard method of determining the valence band edge from photoelectron spectroscopy (XPS and UPS). Furthermore, it shows that a correction to UPS/XPS, based on a parabolic DOS model, developed by Miller et al.[20] predicts the PbS CQD valence band edge size dependence far more accurately.

Chapter 5

Conclusion

The size-dependent quantum confinement effect CQDs provides a unique tunability of the bandgap, which offers many possibilities for optoelectronic devices, such as solar cells. However, for efficient design of devices with PbS CQDs it is important to understand how the properties of of the CQDs change with CQD size. In this work we presented the fabrication and characterization of bilayer heterojunction CQD PbS:C_{60} solar cells fabricated with different sized CQDS, which allowed us to study size-dependent optoelectronic properties of the PbS CQDs.

Even though the quasi-Fermi level of the electrons in these solar cells is limited by the fixed LUMO of the C_{60}, we found that the open-circuit voltage (V_{oc}) strongly depends upon the CQD bandgap. This decrease in V_{oc}, from 0.60 ± 0.02V to 0.35 ± 0.01V for a decrease in CQD bandgaps from 1.53 eV to 0.81 eV, is therefore due to either an increase in recombination or due to a shift of the CQD valence band edge with CQD bandgap.

From transient photovoltage measurements on solar cells with different sized PbS CQDs we induced the charge carrier decay time, which is inversely proportional to the recombination rate. The charge carrier decay times of the solar cells studied here differ by less than an order of magnitude, slightly decreasing upon increasing CQD bandgap. This trend in decreasing decay time upon increasing bandgap is the opposite of the trend required to explain the strongly increasing V_{oc} with increasing bandgap.

The decrease in V_{oc} therefore suggests that the valence band edge level of the PbS CQDs strongly depends on CQD size. However, data from XPS and UPS, both well established methods for the determination of the valence band edge level in semiconductors, shows that for PbS and PbSe CQDs the valence band edge changes only marginally with CQD size[40,47]. This relatively marginal dependence of the valence band edge with CQD size is surprising since the effective masses of electrons and holes are similar in PbS and PbSe. Also, the marginal

dependence of of the valence band edge does not, for example, occur for CdS and CdSe CQDs, were the valence band edge and conduction band edge change comparatively.

The PbS CQD valence band edge change from UPS measurements does not agree the V_{oc} change in our solar cells. However, the V_{oc} change does agree with the valence band edge change of PbS CQDs as proposed by Miller et al.[20], who argue that in lead based CQDs the standard analysis of UPS and XPS is incorrect due to a long low-intensity tail in the density of states that depends on CQD size. Our data on the V_{oc} change of PbS CQD solar cells corresponds with the valence band edge change from the corrected XPS/UPS measurements by Miller et al. and with the same correction applied to UPS data from Jasieniak et al.[40]. Additionally, the measured V_{oc} size dependence is in agreement with a method to determine valence band edge of PbS CQDs with field effect transistors and ab-initio calculations developed by Bisri et al.[69]. Considering the importance of accurate determination of the PbS CQD energetics for device engineering and modeling, we find that the standard analyses of UPS/XPS measurements is not ideal for determining the valence band edge of PbS CQDs. The agreement of our results with the correction by Miller et al. applied to this standard analyses, however, is excellent and suggests a solution to the inaccuracy of the standard UPS/XPS analyses for PbS CQDs. This finding has important implications for determination of the valence band edge with UPS and XPS measurements on PbS CQD films and requires further investigations.

References

[1] N. Panwar, S. Kaushik, and S. Kothari, "Role of renewable energy sources in environmental protection: a review," *Renewable and Sustainable Energy Reviews*, vol. 15, no. 3, pp. 1513–1524, 2011.

[2] E. H. Sargent, "Colloidal quantum dot solar cells," *Nature Photonics*, vol. 6, no. 3, pp. 133–135, 2012.

[3] W. Shockley and H. J. Queisser, "Detailed balance limit of efficiency of p-n junction solar cells," *Journal of Applied Physics*, vol. 32, no. 3, pp. 510–519, 1961.

[4] K. Yoshikawa, H. Kawasaki, W. Yoshida, T. Irie, K. Konishi, K. Nakano, T. Uto, D. Adachi, M. Kanematsu, H. Uzu, *et al.*, "Silicon heterojunction solar cell with interdigitated back contacts for a photoconversion efficiency over 26%," *Nature Energy*, vol. 2, p. 17032, 2017.

[5] E. H. Sargent, "Infrared photovoltaics made by solution processing," *Nature Photonics*, vol. 3, no. 6, pp. 325–331, 2009.

[6] X. Wang, G. I. Koleilat, J. Tang, H. Liu, I. J. Kramer, R. Debnath, L. Brzozowski, D. A. R. Barkhouse, L. Levina, S. Hoogland, *et al.*, "Tandem colloidal quantum dot solar cells employing a graded recombination layer," *Nature Photonics*, vol. 5, no. 8, pp. 480–484, 2011.

[7] G. H. Carey, A. L. Abdelhady, Z. Ning, S. M. Thon, O. M. Bakr, and E. H. Sargent, "Colloidal quantum dot solar cells," *Chemical Reviews*, vol. 115, no. 23, pp. 12732–12763, 2015.

[8] M. Liu, O. Voznyy, R. Sabatini, F. P. G. de Arquer, R. Munir, A. H. Balawi, X. Lan, F. Fan, G. Walters, A. R. Kirmani, *et al.*, "Hybrid organic-inorganic inks flatten the energy landscape in colloidal quantum dot solids," *Nature Materials*, 2016.

[9] S. M. Thon, A. H. Ip, O. Voznyy, L. Levina, K. W. Kemp, G. H. Carey, S. Masala, and E. H. Sargent, "Role of bond adaptability in the passivation of colloidal quantum dot solids," *ACS nano*, vol. 7, no. 9, pp. 7680–7688, 2013.

[10] X. Lan, O. Voznyy, A. Kiani, F. P. García de Arquer, A. S. Abbas, G.-H. Kim, M. Liu, Z. Yang, G. Walters, J. Xu, *et al.*, "Passivation using molecular halides increases quantum dot solar cell performance," *Advanced Materials*, vol. 28, no. 2, pp. 299–304, 2016.

[11] Z. Ning, O. Voznyy, J. Pan, S. Hoogland, V. Adinolfi, J. Xu, M. Li, A. R. Kirmani, J.-P. Sun, J. Minor, *et al.*, "Air-stable n-type colloidal quantum dot solids," *Nature Materials*, vol. 13, no. 8, pp. 822–828, 2014.

[12] A. H. Ip, S. M. Thon, S. Hoogland, O. Voznyy, D. Zhitomirsky, R. Debnath, L. Levina, L. R. Rollny, G. H. Carey, A. Fischer, *et al.*, "Hybrid passivated colloidal quantum dot solids," *Nature Nanotechnology*, vol. 7, no. 9, pp. 577–582, 2012.

[13] X. Lan, O. Voznyy, F. P. Garcia de Arquer, M. Liu, J. Xu, A. H. Proppe, G. Walters, F. Fan, H. Tan, M. Liu, *et al.*, "10.6% certified colloidal quantum dot solar cells via solvent-polarity-engineered halide passivation," *Nano Letters*, vol. 16, no. 7, pp. 4630–4634, 2016.

[14] I. J. Kramer and E. H. Sargent, "The architecture of colloidal quantum dot solar cells: materials to devices," *Chemical reviews*, vol. 114, no. 1, pp. 863–882, 2013.

[15] D. A. R. Barkhouse, R. Debnath, I. J. Kramer, D. Zhitomirsky, A. G. Pattantyus-Abraham, L. Levina, L. Etgar, M. Grätzel, and E. H. Sargent, "Depleted bulk heterojunction colloidal quantum dot photovoltaics," *Advanced Materials*, vol. 23, no. 28, pp. 3134–3138, 2011.

[16] C.-H. M. Chuang, P. R. Brown, V. Bulović, and M. G. Bawendi, "Improved performance and stability in quantum dot solar cells through band alignment engineering," *Nature materials*, vol. 13, no. 8, pp. 796–801, 2014.

[17] M. Liu, F. de Arquer, Y. Li, X. Lan, G.-H. Kim, O. Voznyy, L. K. Jagadamma, A. S. Abbas, S. Hoogland, Z. Lu, *et al.*, "Double-sided junctions enable high-performance colloidal-quantum-dot photovoltaics," *Advanced Materials*, vol. 28, no. 21, pp. 4142–4148, 2016.

[18] A. Polman, M. Knight, E. C. Garnett, B. Ehrler, and W. C. Sinke, "Photovoltaic materials: Present efficiencies and future challenges," *Science*, vol. 352, no. 6283, p. aad4424, 2016.

[19] H. Borchert, *Solar cells based on colloidal nanocrystals*. Springer, 2014.

[20] E. M. Miller, D. M. Kroupa, J. Zhang, P. Schulz, A. R. Marshall, A. Kahn, S. Lany, J. M. Luther, M. C. Beard, C. L. Perkins, *et al.*, "Revisiting the valence and conduction band size dependence of PbS quantum dot thin films," *ACS Nano*, vol. 10, no. 3, pp. 3302–3311, 2016.

[21] S. R. Wenham, M. A. Green, M. E. Watt, R. Corkish, and A. Sproul, "Applied photovoltaics, 2007," *Earthscan, UK*.

[22] R. Debnath, O. Bakr, and E. H. Sargent, "Solution-processed colloidal quantum dot photovoltaics: A perspective," *Energy & Environmental Science*, vol. 4, no. 12, pp. 4870–4881, 2011.

[23] J. Tang and E. H. Sargent, "Infrared colloidal quantum dots for photovoltaics: fundamentals and recent progress," *Advanced Materials*, vol. 23, no. 1, pp. 12–29, 2011.

[24] M. Yuan, M. Liu, and E. H. Sargent, "Colloidal quantum dot solids for solution-processed solar cells," *Nature Energy*, vol. 1, p. 16016, 2016.

[25] R. Saran and R. J. Curry, "Lead sulphide nanocrystal photodetector technologies," *Nature Photonics*, vol. 10, no. 2, pp. 81–92, 2016.

[26] F. P. G. de Arquer, A. Armin, P. Meredith, and E. H. Sargent, "Solution-processed semiconductors for next-generation photodetectors," *Nature Reviews Materials*, vol. 2, p. 16100, 2017.

[27] Y. Shirasaki, G. J. Supran, M. G. Bawendi, and V. Bulović, "Emergence of colloidal quantum-dot light-emitting technologies," *Nature Photonics*, vol. 7, no. 1, pp. 13–23, 2013.

[28] C. R. Kagan, E. Lifshitz, E. H. Sargent, and D. V. Talapin, "Building devices from colloidal quantum dots," *Science*, vol. 353, no. 6302, p. aac5523, 2016.

[29] W. Zhou and J. J. Coleman, "Semiconductor quantum dots," *Current Opinion in Solid State and Materials Science*, vol. 20, no. 6, pp. 352 – 360, 2016. the {COSSMS} Twentieth Anniversary IssueIn celebration of 20 years.

[30] I. Kang and F. W. Wise, "Electronic structure and optical properties of PbS and PbSe quantum dots," *Journal of the Optical Society of America B*, vol. 14, no. 7, pp. 1632–1646, 1997.

[31] H. Choi, J.-H. Ko, Y.-H. Kim, and S. Jeong, "Steric-hindrance-driven shape transition in PbS quantum dots: understanding size-dependent stability," *Journal of the American Chemical Society*, vol. 135, no. 14, pp. 5278–5281, 2013.

[32] I. Moreels, Y. Justo, B. De Geyter, K. Haustraete, J. C. Martins, and Z. Hens, "Size-tunable, bright, and stable PbS quantum dots: a surface chemistry study," *Acs Nano*, vol. 5, no. 3, pp. 2004–2012, 2011.

[33] C. B. Murray, S. Sun, W. Gaschler, H. Doyle, T. A. Betley, and C. R. Kagan, "Colloidal synthesis of nanocrystals and nanocrystal superlattices," *IBM Journal of Research and Development*, vol. 45, no. 1, pp. 47–56, 2001.

[34] J. Zhang, R. W. Crisp, J. Gao, D. M. Kroupa, M. C. Beard, and J. M. Luther, "Synthetic conditions for high-accuracy size control of PbS quantum dots," *The Journal of Physical Chemistry Letters*, vol. 6, no. 10, pp. 1830–1833, 2015.

[35] S. A. McDonald, G. Konstantatos, S. Zhang, P. W. Cyr, E. J. Klem, L. Levina, and E. H. Sargent, "Solution-processed PbS quantum dot infrared photodetectors and photovoltaics," *Nature Materials*, vol. 4, no. 2, pp. 138–142, 2005.

[36] K. W. Johnston, A. G. Pattantyus-Abraham, J. P. Clifford, S. H. Myrskog, D. D. MacNeil, L. Levina, and E. H. Sargent, "Schottky-quantum dot photovoltaics for efficient infrared power conversion," *Applied Physics Letters*, vol. 92, no. 15, p. 151115, 2008.

[37] N. Zhao, T. P. Osedach, L.-Y. Chang, S. M. Geyer, D. Wanger, M. T. Binda, A. C. Arango, M. G. Bawendi, and V. Bulovic, "Colloidal PbS quantum dot solar cells with high fill factor," *ACS nano*, vol. 4, no. 7, pp. 3743–3752, 2010.

[38] S. Tsang, H. Fu, R. Wang, J. Lu, K. Yu, and Y. Tao, "Highly efficient cross-linked PbS nanocrystal/C60 hybrid heterojunction photovoltaic cells," *Applied Physics Letters*, vol. 95, no. 18, p. 183505, 2009.

[39] S. A. Chambers, T. Droubay, T. C. Kaspar, and M. Gutowski, "Experimental determination of valence band maxima for SrTiO3, TiO2, and SrO and the associated valence band offsets with Si (001)," *Journal of Vacuum Science & Technology B: Microelectronics and Nanometer Structures Processing, Measurement, and Phenomena*, vol. 22, no. 4, pp. 2205–2215, 2004.

[40] J. Jasieniak, M. Califano, and S. E. Watkins, "Size-dependent valence and conduction band-edge energies of semiconductor nanocrystals," *ACS nano*, vol. 5, no. 7, pp. 5888–5902, 2011.

[41] B.-R. Hyun, Y.-W. Zhong, A. C. Bartnik, L. Sun, H. D. Abruna, F. W. Wise, J. D. Goodreau, J. R. Matthews, T. M. Leslie, and N. F. Borrelli, "Electron injection from colloidal PbS quantum dots into titanium dioxide nanoparticles," *ACS Nano*, vol. 2, no. 11, pp. 2206–2212, 2008.

[42] V. Colvin, A. Alivisatos, and J. Tobin, "Valence-band photoemission from a quantum-dot system," *Physical Review Letters*, vol. 66, no. 21, p. 2786, 1991.

[43] T. Van Buuren, L. Dinh, L. Chase, W. Siekhaus, and L. J. Terminello, "Changes in the electronic properties of Si nanocrystals as a function of particle size," *Physical Review Letters*, vol. 80, no. 17, p. 3803, 1998.

[44] C. Wang, M. Shim, and P. Guyot-Sionnest, "Electrochromic nanocrystal quantum dots," *Science*, vol. 291, no. 5512, pp. 2390–2392, 2001.

[45] B. Hou, Y. Cho, B. S. Kim, J. Hong, J. B. Park, S. J. Ahn, J. I. Sohn, S. Cha, and J. M. Kim, "Highly monodispersed PbS quantum dots for outstanding cascaded-junction solar cells," *ACS Energy Letters*, vol. 1, no. 4, p. 834, 2016.

[46] G.-H. Kim, F. P. García de Arquer, Y. J. Yoon, X. Lan, M. Liu, O. Voznyy, Z. Yang, F. Fan, A. H. Ip, P. Kanjanaboos, *et al.*, "High-efficiency colloidal quantum dot photovoltaics via robust self-assembled monolayers," *Nano Letters*, 2015.

[47] P. R. Brown, D. Kim, R. R. Lunt, N. Zhao, M. G. Bawendi, J. C. Grossman, and V. Bulovic, "Energy level modification in lead sulfide quantum dot thin films through ligand exchange," *ACS Nano*, vol. 8, no. 6, pp. 5863–5872, 2014.

[48] D. Dissanayake, R. A. Hatton, T. Lutz, C. E. Giusca, R. J. Curry, and S. Silva, "A PbS nanocrystal-C60 photovoltaic device for infrared light harvesting," *Applied Physics Letters*, vol. 91, no. 13, p. 133506, 2007.

[49] J. Endres, D. A. Egger, M. Kulbak, R. A. Kerner, L. Zhao, S. H. Silver, G. Hodes, B. P. Rand, D. Cahen, L. Kronik, *et al.*, "Valence and conduction band densities of states of metal halide perovskites: a combined experimental–theoretical study," *The Journal of Physical Chemistry Letters*, vol. 7, no. 14, pp. 2722–2729, 2016.

[50] S. Olthof, "Research update: The electronic structure of hybrid perovskite layers and their energetic alignment in devices," *APL Materials*, vol. 4, no. 9, p. 091502, 2016.

[51] R. L. Hoye, P. Schulz, L. T. Schelhas, A. M. Holder, K. H. Stone, J. D. Perkins, D. Vigil-Fowler, S. Siol, D. O. Scanlon, A. Zakutayev, *et al.*, "Perovskite-inspired photovoltaic materials: Toward best practices in materials characterization and calculations," *Chemistry of Materials*, 2017.

[52] A. R. Kirmani, A. Kiani, M. M. Said, O. Voznyy, N. Wehbe, G. Walters, S. Barlow, E. H. Sargent, S. R. Marder, and A. Amassian, "Remote molecular doping of colloidal quantum dot photovoltaics," *ACS Energy Letters*, vol. 1, no. 5, pp. 922–930, 2016.

[53] D. Dissanayake, R. A. Hatton, T. Lutz, R. Curry, and S. Silva, "The fabrication and analysis of a PbS nanocrystal: C60 bilayer hybrid photovoltaic system," *Nanotechnology*, vol. 20, no. 24, p. 245202, 2009.

[54] A. Gocalinska, M. Saba, F. Quochi, M. Marceddu, K. Szendrei, J. Gao, M. A. Loi, M. Yarema, R. Seyrkammer, W. Heiss, *et al.*, "Size-dependent electron transfer from colloidal PbS nanocrystals to fullerene," *The Journal of Physical Chemistry Letters*, vol. 1, no. 7, pp. 1149–1154, 2010.

[55] E. Klem, C. Gregory, G. Cunningham, S. Hall, D. Temple, and J. Lewis, "Planar PbS quantum dot/C60 heterojunction photovoltaic devices with 5.2% power conversion efficiency," *Applied Physics Letters*, vol. 100, no. 17, p. 173109, 2012.

[56] W. Yoon, J. E. Boercker, M. P. Lumb, D. Placencia, E. E. Foos, and J. G. Tischler, "Enhanced open-circuit voltage of PbS nanocrystal quantum dot solar cells," *Scientific reports*, vol. 3, p. 2225, 2013.

[57] M. A. Hines and G. D. Scholes, "Colloidal pbs nanocrystals with size-tunable near-infrared emission: observation of post-synthesis self-narrowing of the particle size distribution," *Advanced Materials*, vol. 15, no. 21, pp. 1844–1849, 2003.

[58] R. L. Hoye, B. Ehrler, M. L. Böhm, D. Muñoz-Rojas, R. M. Altamimi, A. Y. Alyamani, Y. Vaynzof, A. Sadhanala, G. Ercolano, N. C. Greenham, *et al.*, "Improved open-circuit voltage in ZnO–PbSe quantum dot solar cells by understanding and reducing losses arising from the ZnO conduction band tail," *Advanced Energy Materials*, vol. 4, no. 8, 2014.

[59] W. M. Lin, D. Bozyigit, O. Yarema, and V. Wood, "Transient photovoltage measurements in nanocrystal-based solar cells," *The Journal of Physical Chemistry C*, vol. 120, no. 23, pp. 12900–12908, 2016.

[60] A. Sundqvist, O. J. Sandberg, M. Nyman, J.-H. Smått, and R. Österbacka, "Origin of the s-shaped J-V curve and the light-soaking issue in inverted organic solar cells," *Advanced Energy Materials*, 2016.

[61] J. Gao, J. M. Luther, O. E. Semonin, R. J. Ellingson, A. J. Nozik, and M. C. Beard, "Quantum dot size dependent J-V characteristics in heterojunction ZnO/PbS quantum dot solar cells," *Nano letters*, vol. 11, no. 3, pp. 1002–1008, 2011.

[62] J. Bisquert, D. Cahen, G. Hodes, S. Rühle, and A. Zaban, "Physical chemical principles of photovoltaic conversion with nanoparticulate, mesoporous dye-sensitized solar cells," *The Journal of Physical Chemistry B*, vol. 108, no. 24, pp. 8106–8118, 2004.

[63] P. P. Boix, M. M. Wienk, R. A. Janssen, and G. Garcia-Belmonte, "Open-circuit voltage limitation in low-bandgap diketopyrrolopyrrole-based polymer solar cells processed from different solvents," *The Journal of Physical Chemistry C*, vol. 115, no. 30, pp. 15075–15080, 2011.

[64] G. Garcia-Belmonte and J. Bisquert, "Open-circuit voltage limit caused by recombination through tail states in bulk heterojunction polymer-fullerene solar cells," *Applied physics letters*, vol. 96, no. 11, p. 48, 2010.

[65] J. J. Choi, C. R. Bealing, K. Bian, K. J. Hughes, W. Zhang, D.-M. Smilgies, R. G. Hennig, J. R. Engstrom, and T. Hanrath, "Controlling nanocrystal superlattice symmetry and shape-anisotropic interactions through variable ligand surface coverage," *Journal of the American Chemical Society*, vol. 133, no. 9, pp. 3131–3138, 2011.

[66] H. Chung, H. Choi, D. Kim, S. Jeong, and J. Kim, "Size dependence of excitation-energy-related surface trapping dynamics in pbs quantum dots," *The Journal of Physical Chemistry C*, vol. 119, no. 13, pp. 7517–7524, 2015.

[67] E. Kraut, R. Grant, J. Waldrop, and S. Kowalczyk, "Precise determination of the valence-band edge in x-ray photoemission spectra: Application to measurement of semiconductor interface potentials," *Physical Review Letters*, vol. 44, no. 24, p. 1620, 1980.

[68] I. Moreels, K. Lambert, D. Smeets, D. De Muynck, T. Nollet, J. C. Martins, F. Vanhaecke, A. Vantomme, C. Delerue, G. Allan, *et al.*, "Size-dependent optical properties of colloidal PbS quantum dots," *ACS Nano*, vol. 3, no. 10, pp. 3023–3030, 2009.

[69] S. Z. Bisri, E. Degoli, N. Spallanzani, G. Krishnan, B. J. Kooi, C. Ghica, M. Yarema, W. Heiss, O. Pulci, S. Ossicini, *et al.*, "Determination of the electronic energy levels of colloidal nanocrystals using field-effect transistors and ab-initio calculations," *Advanced Materials*, vol. 26, no. 32, pp. 5639–5645, 2014.